

MORPHOLOGICAL PARAMETERS OF SPITZER SURVEY OF STELLAR STRUCTURE IN GALAXIES

B.W. HOLWERDA¹ J.-C. MUÑOZ-MATEOS², S. COMERÓN³, S. MEIDT⁴, K. SHETH^{2,5,6}, S. LAINE⁶, J. L. HINZ⁷, M. W. REGAN⁸, A. GIL DE PAZ⁹, K. MENÉNDEZ-DELMESTRE¹⁰, M. SEIBERT¹⁰, T. KIM^{2,11}, T. MIZUSAWA⁴, E. LAURIKAINEN^{3,12}, H. SALO³, J. LAINE³, D. A. GADOTTI¹³, D. ZARITSKY⁷, S. ERROZ-FERRER^{14,15}, L. C. HO¹⁰, J. H. KNAPEN^{14,15}, E. ATHANASSOULA¹⁶, A. BOSMA¹⁶, AND N. PIRZKAL⁸

ABSTRACT

The morphology of galaxies can be quantified to some degree using a set of scale-invariant parameters. Concentration (C), Asymmetry (A), Smoothness (S), the Gini index (G), relative contribution of the brightest pixels to the second order moment of the flux (M_{20}), ellipticity (E), and the Gini index of the second order moment (G_M) have all been applied to morphologically classify galaxies at various wavelengths. Here we present a catalog of these parameters for the *Spitzer* Survey of Stellar Structure in Galaxies (S⁴G), a volume-limited near-infrared imaging survey of nearby galaxies using the 3.6 and 4.5 μm channels of the IRAC camera onboard *Spitzer Space Telescope*. Our goal is to provide a reference catalog of near-infrared quantified morphology for high-redshift studies and galaxy evolution models with enough detail to resolve stellar mass morphology. We explore where normal, non-interacting galaxies –those typically found on the Hubble tuning fork– lie in this parameter space and show that there is a tight relation between Concentration (C_{82}) and M_{20} for normal galaxies. M_{20} can be used to classify galaxies into earlier and later types (e.g., to separate spirals from irregulars). Several criteria using these parameters exist to select systems with a disturbed morphology, i.e., those that appear to be undergoing a tidal interaction. We examine the applicability of these criteria to *Spitzer* near-infrared imaging. We find that four relations, based on the parameters A and S, G and M_{20} , G_M , and C and M_{20} , respectively, select outliers in the morphological parameter space, but each selects different subsets of galaxies. Two criteria ($G_M > 0.6$, $G > -0.115 \times M_{20} + 0.384$) seem most appropriate to identify possible mergers and the merger fraction in near-infrared surveys. We find no strong relation between lopsidedness and most of these morphological parameters, except for a weak dependence of lopsidedness on Concentration and M_{20} .

Subject headings: galaxies: general galaxies: elliptical and lenticular, cD galaxies: spiral galaxies: structure galaxies: statistics galaxies: irregular galaxies: stellar content

¹ European Space Agency Research Fellow (ESTEC), Keplerlaan 1, 2200 AG Noordwijk, The Netherlands, email: benne.holwerda@esa.int or benne.holwerda@gmail.com, twitter: @benneholwerda

² National Radio Astronomy Observatory/NAASC, 520 Edgemont Road, Charlottesville, VA 22903, USA

³ Astronomy Division, Department of Physical Sciences, FIN-90014 University of Oulu, P.O. Box 3000, Oulu, Finland

⁴ Max-Planck-Institut für Astronomie / Königstuhl 17 D-69117, Heidelberg, Germany

⁵ Spitzer Science Center, 1200 East California Boulevard, Pasadena, CA 91125, USA

⁶ Spitzer Science Center, Mail Stop 220-6, 1200 East California Boulevard, Pasadena, CA 91125, USA

⁷ Steward Observatory, University of Arizona, 933 North Cherry Avenue, Tucson, AZ 85721, USA

⁸ Space Telescope Science Institute, 3700 San Martin Drive, Baltimore, MD 21218, USA

⁹ Departamento de Astrofísica, Universidad Complutense de Madrid, 28040 Madrid, Spain

¹⁰ The Observatories of the Carnegie Institution of Washington, 813 Santa Barbara Street, Pasadena, CA 91101, USA

¹¹ Astronomy Program, Department of Physics and Astronomy, Seoul National University, Seoul 151-742, Republic of Korea

¹² Finnish Centre of Astronomy with ESO (FINCA), University of Turku, Vislntie 20, FI-21500, Piikki, Finland

¹³ European Southern Observatory, Casilla 19001, Santiago 19, Chile

¹⁴ Instituto de Astrofísica de Canarias, Vía Láctea s/n 38205 La Laguna, Spain

¹⁵ Departamento de Astrofísica, Universidad de La Laguna, Avda. Astrofísico Francisco Sánchez s/n 38206 La Laguna, Spain

¹⁶ Aix Marseille Université, CNRS, LAM (Laboratoire d'Astrophysique de Marseille) UMR 7326, 13388, Marseille,

1. INTRODUCTION

The formation and evolution of galaxies leave an imprint on their light profile and morphology. Classification of their appearance has mostly been done by eye (see Sandage 2005, for a review) but in recent years there has been a concerted effort to move the classification of visible light images of galaxies to a quantifiable basis. Classical morphological classification has long been done visually. Visual morphological classification is impractical for the very large surveys now underway (an interesting exception is the Galaxy Zoo project, Lintott et al. 2008). Thus the goal is to find a quantifiable morphological classifier.

An obvious classifier is the radial light profile of the galaxy, starting with the distinct profiles of ellipticals and spirals, later more generalized to the Sérsic profile with the power of the profile (n) as the single identifier (Sérsic 1968). However, these profiles ignore much of the small-scale detail in a galaxy image on which human classifiers rely for more subtle distinctions.

Consequently, a range of scale-invariant parameters have been proposed, starting from various concentration indices (Abraham & Merrifield 2000; Conselice 2003), asymmetry (Abraham & Merrifield 2000; Bershadsky et al. 2000), some indicator of smoothness of small-scale structure (Conselice 2003), and later including the Gini inequality parameter (Abraham et al. 2003), the second order moment of the light distribution (Lotz et al. 2004), ellipticity (Scarlata et al. 2007), and G_M , the equality of the second order moment distribution (Holwerda et al. 2011a). The resulting parameter space is hardly mathematically orthogonal or complete but it has seen extensive as well as very specific use. There are clear advantages of simple parameterizations of galaxy morphology: no human biases, practical to implement on millions of objects, the possibility to directly and qualitatively compare across wavelength and redshift or to other characteristics. For example, at higher redshift, there are many galaxies that do not conform to the classical Hubble morphological classification but these can still be qualified using this system. Based on a choice of parameter space and training sample, one can subsequently try to classify galaxies along the Hubble Tuning fork through a machine-learning algorithm (e.g., Lahav et al. 1996; Molinari & Smareglia 1998; Ball et al. 2004; Scarlata et al. 2007; Kormendy & Bender 2012).

Disturbed morphology can be used to identify ongoing galaxy major mergers, and morphological classification parameters have seen much use on galaxy samples observed at low and high redshift to infer the fraction and rate at which galaxies merge (Conselice et al. 2003, 2005, 2008, 2009; Yan et al. 2005; Bundy et al. 2005; Casata et al. 2005; Ravindranath et al. 2006; Scarlata et al. 2007; Trujillo et al. 2007; Lotz et al. 2008; Jogee et al. 2009; Darg et al. 2010; López-Sanjuan et al. 2009a,b). Concurrently, these parameters have shown promise in classifying objects along the Hubble tuning fork, both locally (Conselice 2003; Lotz et al. 2004; Taylor-Mager et al. 2007; Muñoz-Mateos et al. 2009), and at high redshift (Scarlata et al. 2007; Huertas-Company et al. 2009). Meanwhile, efforts using visual inspection and classification by single observers or crowds have kept apace with quantified, automated classifiers (e.g., Darg et al. 2010;

Fortson et al. 2012; Hoyle et al. 2011; Keel et al. 2013; Skibba et al. 2009, 2011, 2012; Masters et al. 2010, 2011, 2012, Holwerda et al. *submitted*).

In this paper, we report our application of the popular morphological parameters to the data of the *Spitzer* Survey of Stellar Structure in Galaxies (S⁴G, Sheth et al. 2010, www.cv.nrao.edu/~ksheth/s4g).

The IRAC camera (Fazio et al. 2004) on board the *Spitzer Space Telescope* (Werner et al. 2004) mostly maps the older stellar population at 3.6 and 4.5 μm and hence stellar mass in these systems (Eskew et al. 2012; Meidt et al. 2012a, 2013, *in preparation*), and IRAC images are much less encumbered by dust extinction than any visible light images¹⁷. Thus, the S⁴G morphological parameterization reveals the underlying stellar mass Hubble type rather than the apparent one, somewhat distorted by dust and star-formation (Buta et al. 2010). The S⁴G sample is one of the largest and uniformly selected and observed in the near-infrared, inviting the possibility of a study of the relations between near-infrared morphology parameters with each other and Hubble type, tidal disturbance, lopsidedness, etc.

Strongly disturbed systems occupy a known sub-space of these morphological parameters. Those selected from this S⁴G sample can be compared to the canonical Arp catalog of disturbed galaxies, to illustrate how well the morphological parameterization selects individual disturbed galaxies.

The aim of S⁴G Survey is to be volume-, mass- and luminosity-limited, using a representative sample of galaxies. It now becomes possible to infer a local volume merger fraction and rate based on the morphological selection of disturbed systems. Our goals are to: (a) describe the S⁴G morphological parameter catalog, (b) explore where the “normal” galaxies lie in this quantified morphology parameter space and explore to what degree these can be morphologically typed based on these parameters, and (c) examine those galaxies that are selected as “disturbed” from this catalog by the various morphological criteria.

Our goal for this paper is to present a uniformly computed catalog of the quantified morphology parameters for the S⁴G survey for which codified morphological classifications from the Third Reference Catalogue (de Vaucouleurs et al. 1991) exist. This quantified morphological catalog will subsequently serve as a reference for higher-redshift surveys where Hubble Types are unknown as well as results from detailed galaxy evolution modeling.

The paper is organized as follows: §2 briefly describes the S⁴G data-products, §3 the morphological parameters, and the application of these parameters to S⁴G. §4 presents the resulting catalogs. §5 discusses the morphological parameters’ relation to Hubble type, §6 discusses those systems that show clear signs of disturbance, §7 discusses the link with lopsidedness, and §8 lists our conclusions.

2. S⁴G DATA

The *Spitzer* Survey of Stellar Structure in Galaxies (S⁴G Sheth et al. 2010) is a volume-, magnitude-, and size-limited ($D < 40$ Mpc, $|b| > 30^\circ$, $m_{B\text{corr}} < 15.5$, $D_{25} > 1'$) survey of 2349 nearby galaxies in 3.6 μm

¹⁷ see also Holwerda et al. (2007a,c)

and 4.5 μm (IRAC channels 1 and 2) of the Infrared Array Camera (IRAC, Fazio et al. 2004) of the *Spitzer Space Telescope* (Werner et al. 2004), using both archival cryogenic- and ongoing warm-mission observations (for a full description and selection criteria, see Sheth et al. 2010). All images have been reprocessed by the S⁴G pipeline. The reprocessed pixel scale is $0''.75$; the resolution is $1''.7$ for 3.6 μm and $1''.6$ for 4.5 μm . Data have been made public (<http://irsa.ipac.caltech.edu/data/SPITZER/S4G/>).

For this paper we use the first and second pipeline products (P1 & P2) of S⁴G (Regan et al. *in preparation*) available from DR1 (January 2013) for 2349 galaxies: the photometry images (*phot*) from P1 and foreground and background object masks from P2 for both the 3.6 and 4.5 μm images (see for more details Sheth et al. 2010). Our morphological parameters are in concert with the final S⁴G data products (Muñoz-Mateos et al., *in preparation*).

S⁴G is designed to be a volume-, luminosity- and especially mass-limited representative sample. Since the initial selection required an HI radial velocity from HyperLEDA (Paturel et al. 2003), early-types are relatively under-represented (Figure 1). In addition, early-types are under-represented because they are typically found in denser environments outside the local volume. The distribution of distances (based on radial velocities) is shown in Figure 2. The majority of our sample is between 10-30 Mpc. The resolution of the Spitzer/IRAC ($\sim 2''$) translates to a physical resolution of less than a kpc over this distance range.

S⁴G observations ideally trace the stellar mass of galaxies in both the 3.6 and 4.5 μm channels (Pahre et al. 2004a,b), with the 3.6 μm considered optimal to study the stellar mass (Zibetti & Groves 2011; Meidt et al. 2012a, 2013, *in preparation*). However, both have known contaminants such as the 3.3 μm PAH feature in the 3.6 μm channel (see the PAH heating models by Bakes et al. (2001)) and contamination from stochastically heated small dust grains in both (Lu et al. 2003; Flagey et al. 2006; Mentuch et al. 2009, 2010). We refer the reader to Meidt et al. (2012a) and Meidt et al. *in preparation* for a comprehensive discussion of the non-stellar and anomalous mass-to-light stellar population contaminating the 3.6 μm channel as a map of stellar mass.

S⁴G has seen use on a variety of galaxy phenomena; disk truncation (Comerón et al. 2012), bar fraction (Sheth et al. *in preparation*), thick disks (Comerón et al. 2011c,b,a), visual and automated morphological classification (Buta et al. 2010, Laine et al. *in preparation*) and Hinz et al. *in preparation*, stellar mass mapping (Meidt et al. 2012a), the role of AGB stars in galaxy appearance (Meidt et al. 2012b), disk lopsidedness (Zaritsky et al. 2013a), and spiral structure (Elmegreen et al. 2011), star-formation hidden in spiral arms (Elmegreen et al. *submitted*), H α kinematics and the stellar disk (Erroz-Ferrer et al. 2012), and Early-type Galaxies with Tidal Debris (Kim et al. 2012).

3. MORPHOLOGY PARAMETERS

In this paper, we use the CAS system (Concentration-Asymmetry-Smoothness) from (Bershady et al. 2000; Conselice et al. 2000), and Conselice (2003), the Gini and M_{20} system from Lotz et al. (2004), and a hybrid

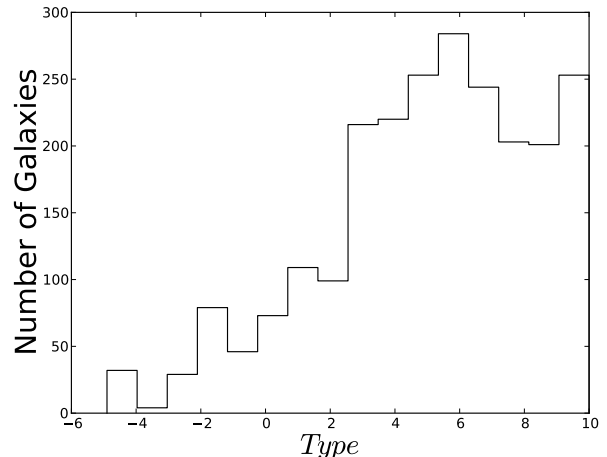


Figure 1. The distribution of galaxy types in our sample of 2349 galaxies from S⁴G. Early-types ($t < 0$) are under-represented in S⁴G.

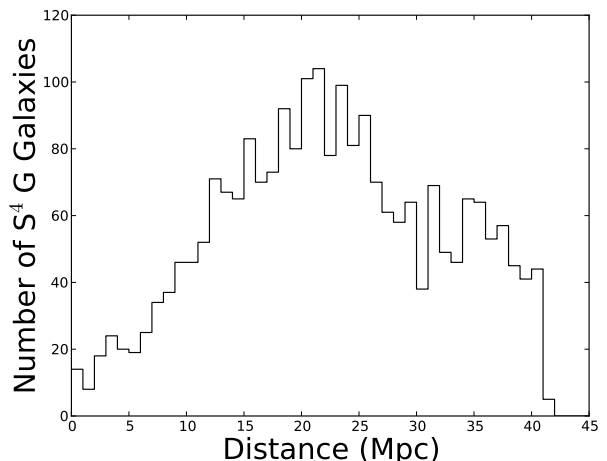


Figure 2. The distribution of galaxy distance ($d = v_{rad}/h_0$) of our sample of 2349 galaxies from S⁴G. Radial velocities from NED where available which means some distances are negative.

parameter G_M , the Gini parameter of the second order moment (Holwerda et al. 2011a).

Concentration is defined as (Kent 1985):

$$C_{82} = 5 \log \left(\frac{r_{80}}{r_{20}} \right), \quad (1)$$

where $r_{\%}$ is the radius of the circular aperture which includes that percentage of the total light of the object. For example, the SDSS generally uses C_{42} , the ratio of the 40% over 20% radii and Scarlata et al. (2007) and Muñoz-Mateos et al. (2009) use the 80% over 20% ratio (C_{82}). We opt to use the C_{82} definition here¹⁸. This

¹⁸ We must note that the earlier version of our code (Holwerda et al. 2011c,d,a,b,e) contained a small error, artificially inflating the concentration values. A quick check revealed this to be $C_{new} = 0.38 \times C_{old}$, and the new, correct values are adopted in this paper, Holwerda et al. (2012), Holwerda et al. *submitted*, and Parekh et

concentration index can be used to quickly discern between light profiles; a de Vaucouleurs profile ($I \propto R^{-4}$) has Concentration value of $C_{82} = 5.2$, and a purely exponential one has a value of $C_{82} = 2.7$. It also can be used to identify unique phenomena, for example HI disk stripping (Holwerda et al. 2011e). In the case of disk galaxies observed in the near-infrared, one can expect this parameter to rise in highly inclined disks: there is more light in the line-of-sight in the center of the galaxy, less obstructed by dust. Bendo et al. (2007) find a smooth increase in Concentration in the 3.6 μm channel with inclination (their Figure 2) but Holwerda et al. (2011c) find a much more complex relation for HI maps. We derive the inclination from the axes ratio reported in Munoz-Matteos et al. *in preparation* for the 25 mag/arcsec² isophote ($\cos^2(i) = (q^2 - q_0^2)/(1 - q_0^2)$) but find no relation between any of the morphological parameters and the disk inclination (see Figure 15). We choose not to correct for inclination because (a) we not always know the inclination accurately (typically not better than 10°), (b) any correction would necessarily need to assume a template galaxy to derive the inclination from (and by necessity ignore disk thickness) or rely on a 3D galaxy model, and (c) in the case of a comparison to high redshift samples, accurate disk inclinations would not be available. Therefore, we choose not to correct for inclination angle. In effect, we explore apparent rather than intrinsic morphology space, including any effects of viewing angle (e.g., apparent disk ellipticity). Scarlata et al. (2007) adopted such a similar approach, in part because accurate inclinations were not available for their high-redshift sample and the computation of disk inclination are not calibrated with HI observations.

In an image with n pixels with intensities $I(i, j)$ at pixel position (i, j) , and in which the value of the pixel is $I_{180}(i, j)$ in the image rotated by 180°, Asymmetry is defined as (Schade et al. 1995; Conselice 2003):

$$A = \frac{\sum_{i,j} |I(i, j) - I_{180}(i, j)|}{2\sum_{i,j} |I(i, j)|}, \quad (2)$$

We chose to ignore the positive background contribution to asymmetry as the *Spitzer* data have a very high signal to noise and the added asymmetry from sky noise is negligible (see also Holwerda et al. 2011c). Fully symmetric galaxies (e.g., an elliptical) would have very low values of Asymmetry. Even a regular spiral would not show a high value of Asymmetry. For example, a grand-design spiral galaxy’s spiral arms map onto each other with a 180° rotation (the rotational symmetry of galaxies can be used to infer dust extinction in pairs of galaxies, see White & Keel 1992; White et al. 2000; Domingue et al. 2000; Keel & White 2001a,b; Keel et al. 2013; Holwerda et al. 2007b, 2009, 2013; Holwerda & Keel 2013). Small-scale structure (e.g. HII regions) in the arms would however contribute to a higher Asymmetry value for spiral galaxies. Flocculant spirals can be expected to be slightly more Asymmetric still. The highest values of Asymmetry can be found in either irregular galaxies (Irr) or galaxies with strong tidal disruptions, provided the

al. *in preparation*, to bring our results in line with the common definition.

tidal structures are included in the calculation and are relatively bright due to recent triggered star-formation. If the wavelength over which the parameter is computed is less sensitive to star-formation, as is the case with the S⁴G imaging, then the Asymmetry signal of interaction or HII regions in spiral arms can be expected to be lower.

Smoothness (also called Clumpiness in the original Conselice 2003) is defined as:

$$S = \frac{\sum_{i,j} |I(i, j) - I_S(i, j)|}{\sum_{i,j} |I(i, j)|}, \quad (3)$$

where $I_S(i, j)$ is the same pixel in the image after smoothing with a choice of kernel. Smoothness is a parameterized version of the unsharp masking technique Malin (1978) used on photographic plates to identify faint structures. The various definitions employ different smoothing kernels and sizes, the most recent one using a flexible kernel-size of 0.2 Petrosian radius and the boxcar shape. To simplify matters, we chose to use a fixed 3 pixel FWHM Gaussian smoothing for our definition (a 30-300 pc. scale). We note that we use the term "Smoothness" for historical reasons as this has become the de facto designation of this parameter (the CAS scheme), even though an increase in its value means a more clumpy appearance of the image (hence its original designation "clumpiness"). Very smooth galaxies (Ellipticals) have very low values of Smoothness but in other galaxies, the value of the Smoothness parameter depends on the size of the smoothing kernel used. If the kernel’s size correspond to, for example, the width of spiral arms at the distance of the galaxy, then grand design spirals will have relatively high Smoothness values. Alternatively, if the kernel corresponds to large HII regions (common in the HST surveys), both spirals and Irregulars will show higher Smoothness values.

Abraham et al. (2003) and Lotz et al. (2004) introduced the Gini and M_{20} parameters. Both are related to the concentration of the light but the Gini parameter does not assume the brightest pixel is in the geometric center of the galaxy image and the M_{20} parameter is more sensitive to merger signals and does not impose circular symmetry on non-merging galaxies.

The Gini parameter is an economic indicator of equality, i.e., $G=1$, if all the flux is in one pixel, $G=0$, if all the pixels in the object have equal values. We use the implementation from Abraham et al. (2003) and Lotz et al. (2004):

$$G = \frac{1}{\bar{I}n(n-1)} \sum_i (2i - n - 1) |I_i|, \quad (4)$$

where I_i is the intensity of pixel i in an increasing flux-ordered list of the n pixels in the object, and \bar{I} is the mean pixel intensity. Holwerda et al. (*submitted*) find a weak link with Gini and current star-formation.

Lotz et al. (2004) introduce the relative second-order moment (M_{20}) of an object. The second-order moment of a pixel is: $M_i = I_i \times R_i = I_i \times [(x_i - x_c)^2 + (y_i - y_c)^2]$, where I_i is the value of pixel i in the image, and x_i and y_i are the x and y coordinates of that pixel and x_c and y_c are the position of the galaxy’s center. Each pixel value is

weighted with the projected radius away from the galaxy center.

The total second-order moment of an image is defined as:

$$M_{tot} = \Sigma M_i = \Sigma I_i [(x_i - x_c)^2 + (y_i - y_c)^2] \quad (5)$$

When we now rank the pixels by value, we can define the relative second-order moment of the brightest 20% of the flux:

$$M_{20} = \log \left(\frac{\Sigma_i^k M_i}{M_{tot}} \right), \text{ for which } \Sigma_i^k I_i < 0.2 I_{tot} \text{ is true.} \quad (6)$$

where pixel k marks the top 20% point in the flux-ordered pixel-list. Some authors vary the central position (x_c , y_c) to minimize this parameter (Lotz et al. 2004; Bendo et al. 2007), but we treat deviations from this value due to variation in the center as a source of uncertainty.

The M_{20} parameter is a parameter that is sensitive to bright structure away from the center of the galaxy; flux is weighted in favor of the outer parts. It therefore is relatively sensitive to tidal structures (provided of course these are included in the calculation), specifically star-forming regions formed in the outer spiral or tidal arms. If no such structures are in the image, the 20% brightest pixels will most likely be concentrated in the center of the galaxy, which is weighted lower. Thus, one can expect low values of M_{20} for smooth galaxies with bright nucleus (Ellipticals, S0 or Sa) but much higher values (less negative) for galaxies with extended arms featuring bright HII regions. For example, Holwerda et al. (2012) show how the combination of M_{20} and Asymmetry can be used to identify extended ultra-violet disks (e.g., those identified by Thilker et al. 2007). As with the Smoothness parameter, one expects the contributions from star-formation to be much less in S⁴G, lowering contrast of HII regions at higher radii; lower values for M_{20} in galaxies that would have a much higher value in bluer wavebands.

Instead of the intensity of the pixel (I_i) one can use the second order moment of the pixel ($M_i = I_i [(x_i - x_c)^2 + (y_i - y_c)^2]$) in equation 4. This is the G_M parameter (Holwerda et al. 2011a):

$$G_M = \frac{1}{Mn(n-1)} \Sigma_i (2i - n - 1) |M_i|, \quad (7)$$

which is an indication of the spread of pixel values weighted with the projected radial distance to the galaxy center. In essence this is the Gini parameter with a different weighting scheme than unity for each pixels. Similar to the M_{20} parameter, it emphasizes the flux from the outer regions of the galaxy. If there is significant flux in the outer parts, this will boost the value of G_M . Contrary to M_{20} , it does not depend on a somewhat arbitrary delineation of the brightest 20% flux for the denominator but relies on all pixel values. Unlike the Gini parameter, however, it does rely on a supplied center of the galaxy (to compute M_i). For concentrated galaxies, the G_M and Gini values will be close together but as relatively more flux is evident in the outer parts of the galaxy, G_M will be higher. Holwerda et al. (2011d) found this a good *single* parameter to identify

active mergers (sweeping tidal tails etc.) from atomic hydrogen maps (HI).

Scarlata et al. (2007) added the ellipticity of a galaxy's image to the mix of parameters in order to classify galaxies according to type in the COSMOS field. Ellipticity is defined as:

$$E = 1 - b/a \quad (8)$$

with a and b , the major and minor axes of the galaxy, computed from the spatial second order moments of the light along the x and y axes of the image in the same manner as Source Extractor (Bertin & Arnouts 1996; Holwerda 2005). We include this definition for completeness.

As input for all these parameters we need an estimate of the center of the object and a definition of the area over which they need to be computed. For the object centers, we use the right ascension and declination from Sheth et al. (2010) and we use a limiting surface brightness of 25 mag/arcsec² to include pixels, excluding foreground and background objects masked by the S⁴G pipeline.

3.1. Computation of Morphological Parameters

To compute the morphological parameters, one needs the image, the center of the object and a criterion for which pixels to include. The object center is taken from the S⁴G catalog (Muñoz-Mateos et al. *in preparation*) and pixels are included if they exceed our surface brightness criterion (25 mag/arcsec²) and are not excluded by the P2 masks. We chose a practical limit of 25 mag/arcsec² (AB magnitude) in both bands (Sheth et al. 2010, Muñoz-Mateos et al. *in preparation*). S⁴G is sensitive down to ~ 27 mag_{AB}/arcsec² in both bands, in the case of smoothed isophotes but not individual pixels. We cut out a section of the mosaic corresponding to $5 R_{25} \times 5 R_{25}$, the radius from de Vaucouleurs et al. (1991) around the central position to speed computation.

The use of an isophotal criterion is uncommon in Hubbel Space Telescope (*HST*) surveys of distant galaxies which span large redshifts, since the selected area will be affected by cosmological surface brightness dimming, k-correction, evolution, and zeropoint offsets at different redshifts. For these applications, an aperture with the Petrosian radius is often employed (see Bershady et al. 2000). Muñoz-Mateos et al. (2009) find that an elliptical aperture based on the Petrosian radius misses significant emission in the *Spitzer* Infrared Nearby Galaxy Survey (SINGS, Kennicutt et al. 2003) IRAC images, depending on the concentration of the galaxy (i.e., depending on Hubble Type). Since this is a local volume sample which suffers little from the above-mentioned redshift issues, we opt for an isophote-defined area (all pixels exceeding 25 mag/arcsec²) to fully include all information, while excluding as much sky-noise as practical.

3.2. Uncertainties

Uncertainties in the morphological parameters come from the uncertainty in the position of the center, the image segmentation, and shot noise in the pixel flux values. Potential biases are if the parameter values change also with viewing angle (i.e., disk inclination) and distance to the object. We explore these issues in sections 2 and 3 and Figures 15 and 16 in the the Appendix.

Some authors minimize the parameters –most often Asymmetry– by varying the central position (Bendo et al. 2007; Muñoz-Mateos et al. 2009). However, de Blok et al. (2008) find that the dynamical center and the brightest point in the 3.6 μm light distribution nearly always coincide. Instead of minimizing, we take the central position from the S⁴G catalog as given but then vary this input center with a random Gaussian distribution with FWHM=3 pixels to define the variance in each morphological parameter. This variance then defines a measure of our uncertainty in these parameters.

The second uncertainty relates to the segmentation of the image, i.e., which parts of the image are assigned to the target object, which to other objects or masked because of image artifacts. Depending on crowding of objects in the field, a substantial fraction of the information on an extended object may be lost. DR1 of S⁴G applies uniform criteria to mask objects not belonging to the target galaxy using a combination of a sextractor segmentation image (see also Holwerda 2005) and visual masking by the data team. While a different fraction of the image will be masked for each target galaxy, we can be confident that the masking is self-consistent across the sample.

Our remaining choice is which parts of the image to include as information on the target galaxy, i.e., which pixels contain enough flux from this galaxy to be included and which pixels are mostly background noise? Different authors have solved this in the literature. For example, both Bendo et al. (2007) and Muñoz-Mateos et al. (2009) use an elliptical aperture to define the boundaries on the image over which the morphological parameters are to be computed. The high-redshift studies, however, tend to use an isophotal cutoff, a minimum value or signal-to-noise for pixels to be included. The latter reasoning is that an elliptical aperture may both cut off outlying flux belonging to the target galaxy as well as include areas of near pure noise. Because our goals include to serve as a benchmark for higher redshift surveys, we opt for an isophotal approach. But the choice of both masking and the threshold or aperture will influence the level of noise included in the pixel collection over which the morphological parameters are computed. One solution would be to take a random sub-set of the pixel collection that is the target galaxy and compute the parameters over these. The variance in the parameter values would be an indication how critical the parameters depend on the inclusion of certain pixels. In an extreme case for example, a single saturated pixel could throw all the morphological parameters and the variance would reflect that. However, taking sub-samples would change the signal-to-noise in each sub-set of pixels.

For the majority of parameters the uncertainty is dominated by variance in the input central position and shot noise in the pixels. Computing the variance from sub-samples of pixels would count the pixel shot noise twice. The exception is the Gini parameter, which does not depend on the input central position but critically on the size of the sample¹⁹. Therefore, we use jackknifed (sub-

sampled) Gini values to compute its uncertainty, using a set of ten random subsamples.

The third uncertainty is the Poisson noise in the pixel flux values. We estimate this by randomizing the pixel values around the mean with the same rms as the real pixel collection but keeping the general shape of the pixel collection. This has the advantage of keeping the total information going into the morphological parameter the same but it quantifies the effect of pixel value outliers on the overall parameter value, i.e., a single bright spot skewing the computed value.

The reported uncertainties in Tables 5 and 2 are the quadratic combination of the uncertainty due to variance in the central position and the uncertainty due to shot noise in the pixels. In the case of the Gini parameter, it is the quadratic combination of the uncertainties estimated from subsampling and pixel shot noise. These values are formal uncertainties of these parameters as the viewing angle and distance may still influence the perception of morphology, and affect the morphological parameter values. However, since the viewing angle is arguably part and parcel of a galaxy morphology (e.g., Scarlata et al. (2007) treat it as such) and S⁴G is a sample of local galaxies (as described in the previous section), making distance less of an issue, we leave these effects out of the formal error.

4. MORPHOLOGY CATALOGS

Tables 5 and 2 list the morphological parameters for both IRAC wavelengths (3.6 and 4.5 μm) and their uncertainties for all 2349 galaxies (full tables are available in the *electronic edition* of the paper). We compute the C_{82} concentration index, Asymmetry, Smoothness (after a 3 pixel FWHM Gaussian smooth), the Gini, M_{20} , the Gini of the second order moment (G_M), and the Ellipticity of the images. Uncertainties are based on randomly changing the central position (with the exception of Gini) and a random reshuffle of the pixel values to simulate shot noise. We note that these uncertainties should be viewed as formal errors and do not include the effects of, for example, disk inclination which have a pronounced effect (see also Bendo et al. 2007; Holwerda et al. 2011c). We explore the possibility of an ordered morphological list based on these parameters, and their ability to select out-of-the ordinary or merging morphology in the near-infrared.

5. GALAXY CLASSIFICATION – WHERE NORMAL GALAXIES LIE

As already noted, these parameters do not constitute an orthogonal parameter space, and most often some combination is used to define a sub-space populated by unperturbed galaxies on the Hubble tuning fork, i.e., “normal” galaxies. First we explore each parameter with Hubble type, and subsequently the two-parameter combinations from Lotz et al. (2004) and Conselice (2003).

Normal spaces have been defined for local samples by Conselice (2003) and Lotz et al. (2004) from the visible light image collection originally presented in Frei et al. (1996). Morphological parameters from *Spitzer*-IRAC images for the SINGS sample have been reported by Bendo et al. (2007), Muñoz-Mateos et al. (2009) and Holwerda et al. (2011c). We will compare to each of these studies to explore where normal galaxies reside in

¹⁹ The issue of the Gini parameter’s dependence on signal-to-noise noted by Lisker (2008) is a direct result of the use of an aperture rather than an isophote. However, the S⁴G galaxies are well above the S/N levels discussed by Lisker et al.

Table 1
Legend for the Numerical Hubble types from HyperLEDA
(Paturel et al. 2003).

Hubble	Type
E	-5
E-S0	-3
S0	-2
S0/a	0
Sa	1
Sab	2
Sb	3
Sbc	4
Sc	6
Sc-Irr	8
Irr	10

the morphological parameter space measured at 3.6 and 4.5 μm . In Figures 4–14, we use the RC3 numerical Hubble type (Table 1) from HyperLEDA (Paturel et al. 2003) to color-code the data points. These are visual classifications in bluer wavelength images but their uniformity and numerical scale allow for a quick comparison.

5.1. Single Parameters

Figure 3 shows the relation between Hubble Type (RC, Table 1) and each of the morphological parameters. Concentration, Gini and M_{20} show the most promise for differentiating between Hubble types. No single parameter alone appears discerning enough to quantify Hubble type completely. This has been found previously for visible light morphologies by Lotz et al. (2004); Conselice (2003), and Scarlata et al. (2007). M_{20} appears to have the most differentiating power for Hubble type classification, i.e., this parameter has the steepest dependence on Hubble Type in Figure 3 (see §5.2.3). The Spearman ranking with Hubble Type (Table 2), ranks Concentration, M_{20} , and Gini as reasonably closely linked to Hubble Type (a ranking of 0 is unrelated, -1 anti-correlated and 1 linearly related). The link is stronger with 3.6 μm parameters than 4.5 μm . For comparison, the ranking with stellar mass is also listed in Table 2, showing that the morphological relation is related to total stellar mass as well (from low-mass irregulars to massive ellipticals).

In the M_{20} panel, a clustering is visible near $M_{20} = -1$ for $T > 2$. We inspected the S⁴G images of some examples of these objects. They include many examples of edge-on and barred galaxies. In the case of edge-on galaxies, the line-of-sight integration of stellar light (with little extinction) results in relatively more light at higher galactocentric radii; thus the same Hubble Type has a greater contribution from the top 20% of pixels at greater radii. A similar effect happens if stars are dynamically concentrated in a bar: some of the brightest pixels will occur at higher radii, increasing the value of M_{20} .

5.2. Parameter Pairs

In this section we discuss a few of the parameter pairs, noted in the literature (Conselice 2003; Lotz et al. 2004; Muñoz-Mateos et al. 2009) as useful to separate “normal” galaxies from “disturbed” ones and morphologically classify these “normal” galaxies. For example, figure 17 in the appendix illustrates the distribution of the S⁴G sample over the parameter space. Buta et al. (2010) note

that late-types (S0/a to Sc) galaxies appear earlier in type at 3.6 μm , due to the slightly increased prominence of the bulge and the reduced effects of extinction.

5.2.1. Asymmetry and Smoothness

Conselice (2003) define an Asymmetry–Smoothness relation ($A = 0.35 \times S + 0.02$) for R-band images where normal galaxies reside. Figure 4 shows the relation between Asymmetry and Smoothness. The population is split between two sequences: one where Smoothness follows Asymmetry, mostly populated by irregulars and spirals, and one where these parameters are completely unrelated. Neither case presents a clear separation between early and late types.

In these near-infrared images (and perhaps with our implementation of the parameters) there is little use for this pair as a classifier. One obvious difference between this study and any previous one is the wavelength: in their comparisons between wavelengths in the SINGS/THINGS sample both Muñoz-Mateos et al. (2009) and Holwerda et al. (2011c) find much lower values of Asymmetry for 3.6 μm compared to other, especially optical, wavelengths. The typically lower values of Asymmetry are the cause of the poor separation of early and late types.

We note that our simple implementation of Smoothness, i.e., a fixed-sized smoothing kernel, could be affected by distance effects, but the mean of the Smoothness parameter for a given Hubble Type does not change between nearby and distant subsamples. A more likely reason is that Conselice (2003) use R-band optical images and S⁴G is in the near-infrared with the resulting different dependencies on star-formation and dust extinction.

5.2.2. Gini and M_{20}

Lotz et al. (2004) showed that Gini and M_{20} together separate early from late types based on visible light images. They define a criterion between normal and disturbed galaxies (see equation 14). Figure 5 shows the Gini– M_{20} space for S⁴G. There seems to be a (noisy) sequence between Gini and M_{20} with Hubble type. This correlation reflects the well known trend of an increase in central/bulge prominence from late to early type. Surprisingly, early-types (elliptical and S0) galaxies appear to display a range of Gini values. This is somewhat unusual as these are the smoothest galaxies, with the smallest contribution to the second order moment by the brightest 20% of the flux (M_{20}) because these are all in the center. Several of these are selected as “disturbed” galaxies (see also the discussion of Figure 12 below). However, their pixel values are not homogeneous – each pixel contributing the same fraction of the flux – and thus the Gini parameter becomes akin to a concentration index (Figure 6) as ranking by flux becomes similar to ranking by radius.

Muñoz-Mateos et al. (2009) define an envelope based on the morphology of the SINGS galaxies for the Gini– M_{20} space (dotted lines in the left panel of Figure 5). The S⁴G parameters do not appear to adhere to this envelope. Our implementation is different on two points: first we use an isophotal definition of the pixels to be included and secondly, we include any bright central source in our computation. In Holwerda et al. (2011c), we compared our results to those from Bendo et al. (2007) for the

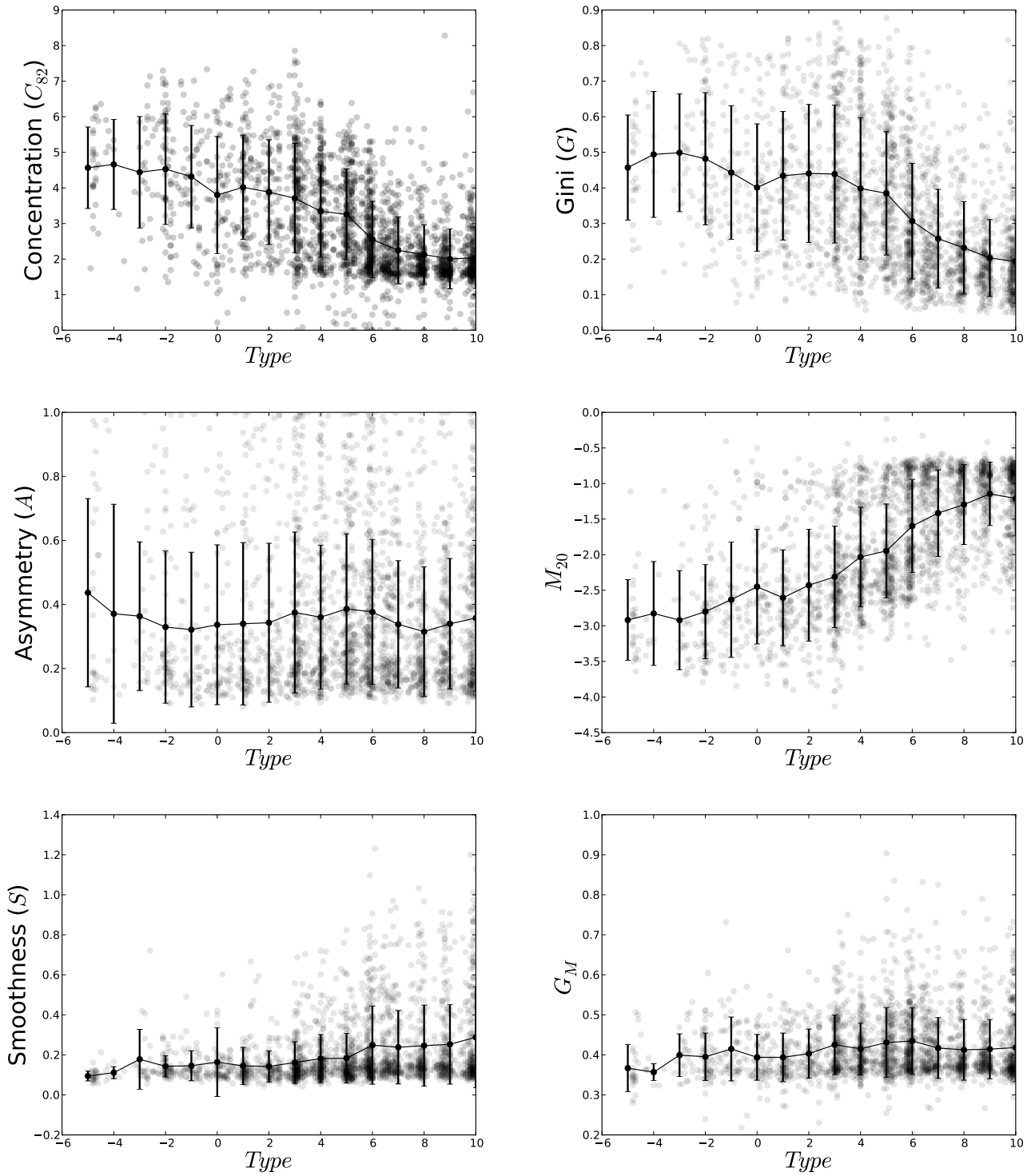


Figure 3. The relation between the Hubble type and each of the morphological parameters in $3.6 \mu\text{m}$. Solid points are the mean value for each Hubble type, the error bars the rms in each type.

Table 2

The Spearman ranking of the relation between Hubble Type or stellar mass with the morphological parameters in either 3.6 μm or 4.5 μm images for our full sample. The absolute z-values of significance for each of Spearman rankings are noted between parentheses.

	C	A	S	M_{20}	G	G_M
3.6 μm						
$\log_{10}(M_*)$	0.11 (3.74)	-0.06 (1.90)	-0.15 (5.25)	-0.08 (2.95)	0.06 (1.94)	-0.09 (3.17)
Hubble Type	-0.55 (29.20)	0.02 (0.88)	0.26 (12.67)	0.62 (33.86)	-0.52 (27.21)	0.05 (2.36)
[3.6 – 4.5]	0.00 (0.08)	0.02 (0.55)	-0.01 (0.39)	0.00 (0.11)	0.00 (0.03)	-0.01 (0.23)
4.5 μm						
$\log_{10}(M_*)$	0.10 (3.57)	-0.03 (1.18)	-0.10 (3.45)	-0.06 (2.01)	0.02 (0.68)	-0.04 (1.37)
Hubble Type	-0.43 (21.69)	-0.05 (2.28)	0.09 (4.04)	0.50 (25.91)	-0.38 (18.81)	-0.06 (2.80)
[3.6 – 4.5]	0.00 (0.01)	0.04 (1.23)	-0.00 (0.13)	-0.02 (0.52)	0.02 (0.53)	0.02 (0.64)

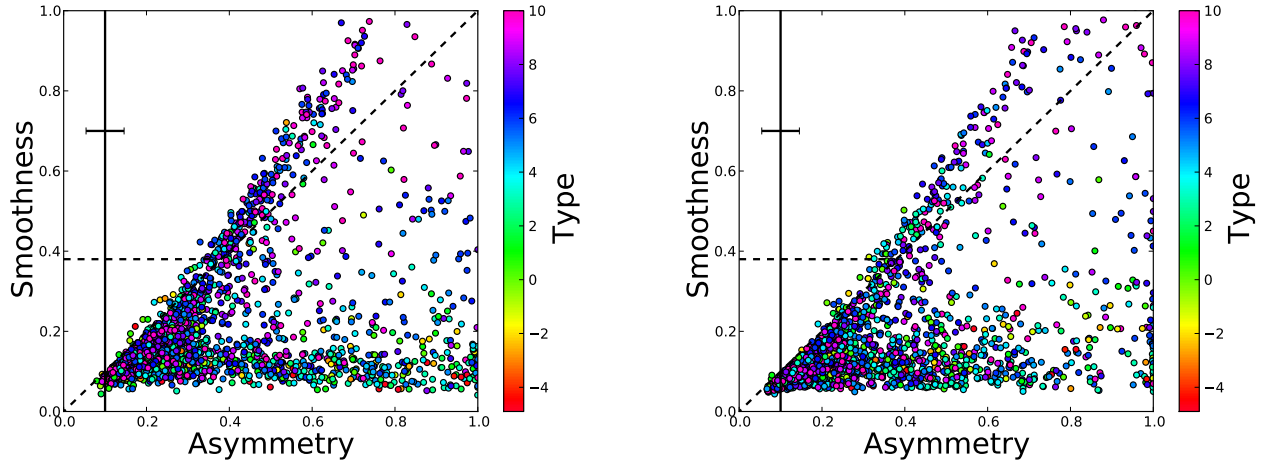


Figure 4. The relation between Asymmetry and Smoothness for 3.6 (left) and 4.5 μm (right) for S⁴G galaxies. The dashed line is Asymmetry-Smoothness equality, a prerequisite for interaction from Conselice (2003) for interacting systems (equation 13). Galaxies above this dashed line and with Asymmetry greater than $A=0.4$ are candidates for ongoing or recent interaction.

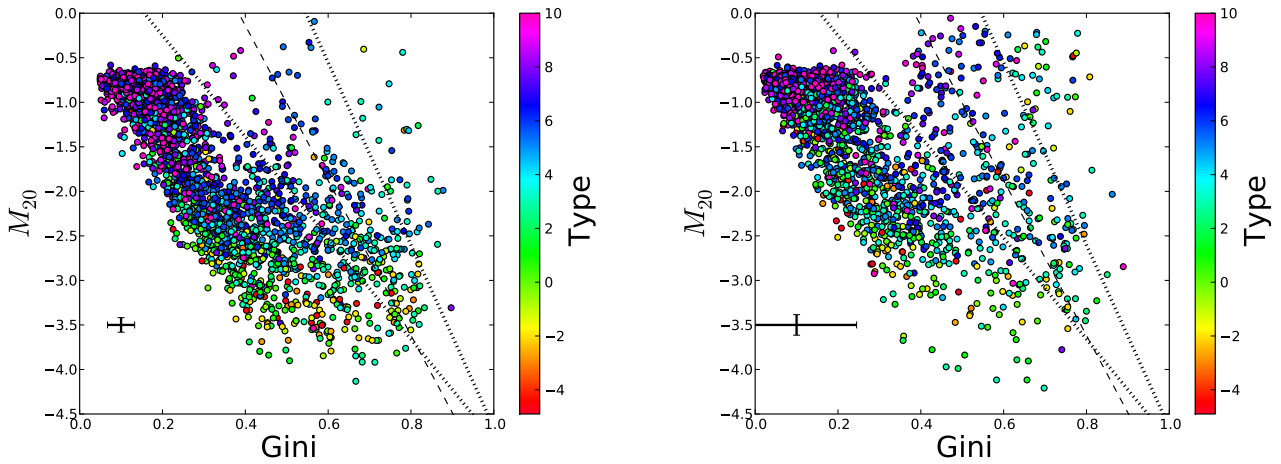


Figure 5. The relation between Gini and M_{20} for 3.6 (left) and 4.5 μm (right) for S⁴G galaxies. The dashed line is the interaction criterion in equation 14 from Lotz et al. (2004) The dotted lines in the 3.6 μm plot are the limits of the envelope from Muñoz-Mateos et al. (2009).

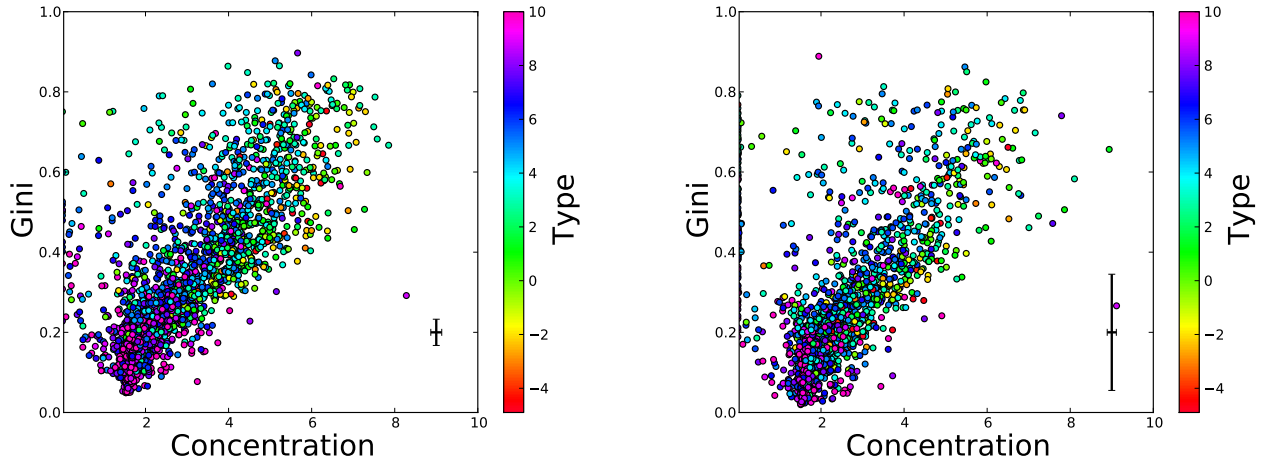


Figure 6. The relation between Concentration and Gini for 3.6 (left) and 4.5 μm (right) for $S^4\text{G}$ galaxies. Points are color-coded according to Hubble Type. Both parameters are closely related for early-types but diverge for late-types as additional structure influences both differently.

SINGS sample, computed over a similar elliptical aperture. There is an offset in the Gini parameter—our Gini values are 0.15 higher—which can be attributed to the convolution of the 3.6 μm images to 24 μm resolution by Bendo et al. (2007). Similarly, Muñoz-Mateos et al. (2009) find that for different apertures, the values of Gini change between the Gini values computed over the R_{25} elliptical aperture and the Petrosian radius elliptical aperture. The difference is ~ 0.1 . Thus, the choice to include central sources, the choice of aperture and thirdly, any convolution, all add a shift to the Gini parameter values for the whole sample.

In Figure 5, we find that the offset in M_{20} is 0.5 lower than those typically found by Muñoz-Mateos et al. (2009), which would be the result of our choice of an isophotal area over an elliptical aperture: M_{tot} is higher as low-flux pixels are excluded, and therefore the relative contribution by the brightest 20% is smaller. A larger number of pixels contributing a small fraction of the total flux would *increase* the value of the Gini parameter. However, the isophotal criterion does away with low contribution pixels and this may explain our lower values for Gini.

5.2.3. Concentration – M_{20}

Originally, Lotz et al. (2004) introduced the M_{20} parameter as a possible alternative to the concentration parameter from Conselice (2003). The definition of M_{20} does not hinge on the placement of circular or elliptical apertures and is thus more sensitive to “any bright nuclei, bars, spiral arms, and off-center star clusters.” Muñoz-Mateos et al. (2009) find a clean relation between C_{82} and M_{20} at 3.6 μm for galaxies in the SINGS sample that represents a clear sequence of Hubble morphologies. Scarlata et al. (2007) also single out the concentration (C_{82}) and M_{20} , as well as Gini- M_{20} combinations for their discriminatory power.

Figure 7 shows the relation between our C_{82} and M_{20} . Obviously the relation is different from the one in Muñoz-Mateos et al. (2009) as we use the same definition of concentration but include any central source. In particular, the 3.6 μm relation is much tighter between these

two parameters than any other pair, with only a few objects that are possibly disturbed galaxies (see below) away from the correlation. A second order polynomial fit between C_{82} and M_{20} at 3.6 μm yields a relation of:

$$M_{20} = -0.0017 \times (C_{82})^2 - 0.47 \times C_{82} - 0.43 \quad (9)$$

and for 4.5 μm :

$$M_{20} = -0.064 \times (C_{82})^2 - 0.04 \times C_{82} - 0.85, \quad (10)$$

after excluding the points above the “disturbed” line. Thus the concentration and M_{20} at both wavelengths are closely related for the majority of the $S^4\text{G}$ galaxies. Figure 8 shows the residual as a function of Hubble Type.

It appears that in the case of the 3.6 and 4.5 μm images, one can define the normal galaxy sequence of C_{82} and M_{20} , and any galaxy with morphology that deviates from this relation by more than 0.5 can be marked as “peculiar”. In the case of the 4.5 μm images, there are many more galaxies that would be marked as peculiar by this selection.

Moreover, we can use the C- M_{20} selection to identify “normal”/unperturbed galaxies, and subsequently classify these using the M_{20} parameter. One potential use of this relation is a check of galaxy models. Typical stellar mass maps should lie on this C_{82} - M_{20} sequence.

We now fit the relation between the Hubble type from HyperLEDA and the M_{20} parameter, after excluding outliers from the Concentration- M_{20} relation. The numerical Hubble type, derived from M_{20} only, either at 3.6 or 4.5 μm , can be expressed as:

$$T(3.6\mu\text{m}) = -0.57 \times (M_{20})^2 - 0.31 \times M_{20} + 7.91, \quad (11)$$

or

$$T(4.5\mu\text{m}) = 0.86 \times (M_{20})^2 - 5.3 \times M_{20} + 10.2, \quad (12)$$

respectively.

Figure 9 shows the Hubble type distribution of M_{20} -selected sub-samples. One can retrieve the broad classifications from *HyperLEDA*, i.e., late- versus early-type galaxies or irregulars from spirals but a more detailed distinction cannot be made using this approach alone.

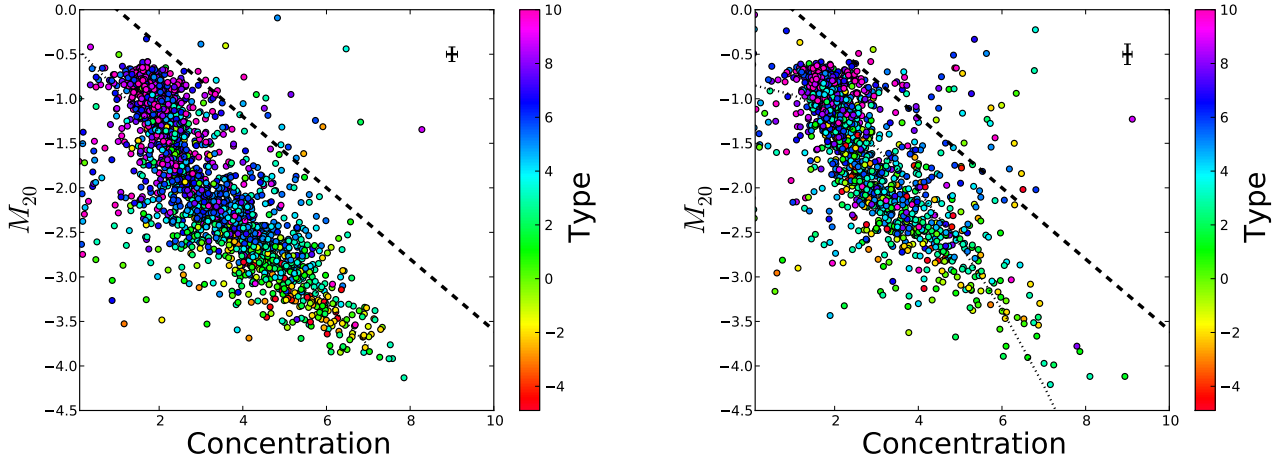


Figure 7. The relation between Concentration and M_{20} for 3.6 (left) and 4.5 μm (right) for S⁴G galaxies. The dashed line is the interaction criterion for optical classification from Lotz et al. (2004) (equation 18) and the dotted line the best fit to the Concentration and M_{20} relation (equations 9 and 10).

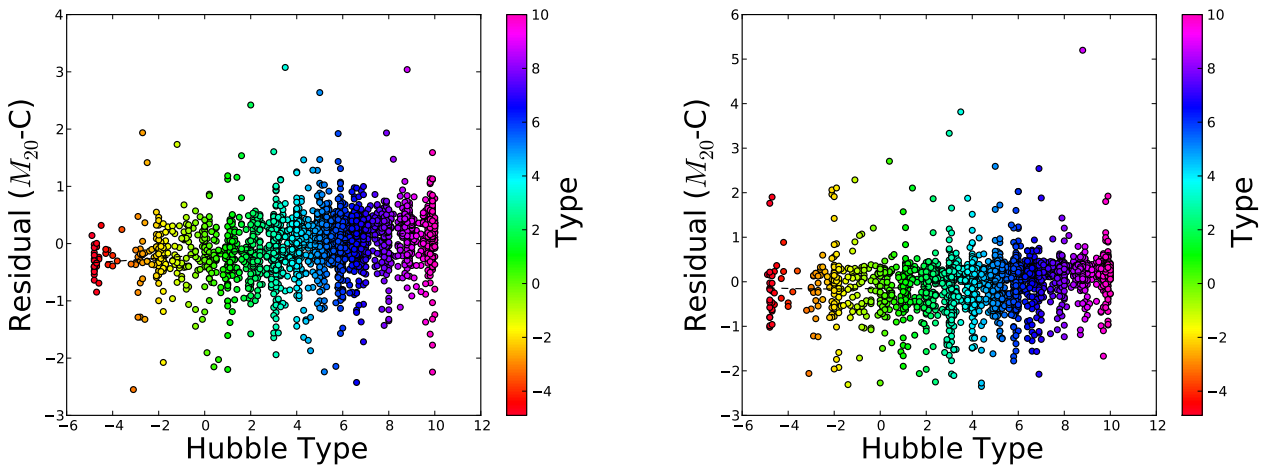


Figure 8. The residual at 3.6 (left) and 4.5 μm (right) for S⁴G galaxies after subtracting the Concentration- M_{20} relations in equations 9 (left) and 10 (right panel).

Given the subjective nature of visual galaxy classifications, one could use this automatically-derived Hubble type as an alternative to catalogs such as RC3 or *HyperLEDA* in future uses of S⁴G or in future near-infrared imaging surveys. As the 3.6 μm relation has the least scatter, we recommend this band for this broad typing in particular.

6. GALAXY CLASSIFICATION – DISTURBED SYSTEMS

There are a few established criteria to select morphologically disturbed galaxies based on these parameters in the literature. These are mostly based on visible light data and select galaxies during the first and second passes of a merger and oftentimes recent merger remnants as well. Here we compare how well such parameters could be applied to the S⁴G near-infrared imaging.

For visible light data, Conselice (2003) define the following criterion:

$$A > 0.38 \text{ and } S > A \quad (13)$$

In general, they consider any highly asymmetric galaxy as a candidate merging system. The vast majority of our galaxies is not disturbed according to this criterion and those selected are classified as late-types (Figure 4). The definition of Smoothness fluctuates somewhat but this may be a viable way to select disturbed or irregular galaxies.

Lotz et al. (2004) added two different criteria using Gini and M_{20} :

$$G > -0.115 \times M_{20} + 0.384 \quad (14)$$

and Gini and Asymmetry:

$$G > -0.4 \times A + 0.66 \text{ or } A > 0.4. \quad (15)$$

The latter is a refinement of the Conselice et al. criterion in equation 13.

The G- M_{20} criterion selects the scatter away from the locus of galaxies which includes a variety of Hubble types (Figure 5). Slope and normalization will have to be ad-

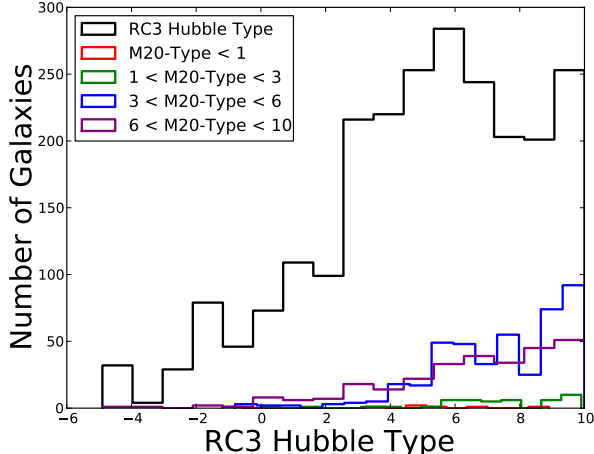


Figure 9. The histogram of Hubble types from the RC3 (de Vaucouleurs et al. 1991) for the complete S⁴G sample and the distribution of RC3 types for different selections of M₂₀-derived types, following equation 11. Those galaxies classified as late-type by equation 11 are in fact late-type according to the RC3 but a finer distinction cannot be made, i.e., Sa from Sc type spirals.

justed to select all the disturbed systems. The bigger spread in Gini parameters for early types (E and S0) for their given M₂₀ value is the cause for this. These early-type “disturbed” systems do indeed include some galaxies with close companions (notably NGC 5195, M51’s companion) but also some S0s with faint spiral structure and especially many S0 galaxies with rings visible in the 3.6 and 4.5 μm images. The second criterion, using Gini and Asymmetry, does not seem to be applicable to the S⁴G data (Figure 10).

Holwerda et al. (2011d) defined some criteria for 21 cm radio data (HI), which has a much lower spatial resolution than S⁴G and show the atomic hydrogen gas, not the stellar content. They define “morphologically disturbed”, based on their G_M parameter, as:

$$G_M > 0.6, \quad (16)$$

or based on Asymmetry and M₂₀:

$$A > -0.2 \times M_{20} + 0.25, \quad (17)$$

or concentration and M₂₀, similar to the criteria from Lotz et al. (2004) (equations 14 and 15). Based on Figure 7, we define a C-M₂₀ criterion for Spitzer imaging, similar to equation 11 in Holwerda et al. (2011a), as:

$$C_{82} > -2.5 \times M_{20} + 1 \quad (18)$$

Of these, the G_M and the C₈₂-M₂₀ criteria seem to be applicable to the S⁴G data (Figures 7 and 11), in the latter case with a slight renormalization. In the latter criterion’s case, 4.5 μm morphology is more often disturbed than the 3.6 μm. One possibility is in our view that in these galaxies there is a hot dust contribution from HII regions to the global morphology of these disks (see §6.3). This leaves us with four criteria that may well select the outlying “disturbed” galaxies.

6.1. What kind of galaxies are selected as disturbed?

Table 3
Morphological Selection Parameters

Criterion	3.6 μm		4.5 μm	
	No.	%	No.	%
$S > A \ \& \ A > 0.38$	600	25.5	574	24.4
$G > -0.115 \times M_{20} + 0.384$	166	7.1	159	6.7
$G_M > 0.6$	76	3.2	185	7.9
$C > -2.5 \times M_{20} + 1$	24	1.0	46	2.0

The four different criteria in Table 3 select different Hubble types as “disturbed”. Figure 12 shows the distribution of Hubble types for the four criteria that seem promising for use on *Spitzer* data to identify disturbed galaxies. The Asymmetry-Smoothness criterion (equation 13) selects many more galaxies than the other criteria, with a preference for spirals. The fact that so many galaxies are selected makes this criterion suspect to use for the selection of unusual or interacting systems. The Gini-M₂₀ criterion (equation 14) also selects a mix of Hubble types, mostly earlier type spirals (Sb or Sc). As noted, the early-types that are selected appear to be a mix of actually interacting galaxies and S0 galaxies with rings or spiral structure. The G_M criterion selects predominantly the latest types (Sc and Irr). The C-M₂₀ criterion (equation 18) selects later types as well. A large fraction of these are edge-on spirals or very faint irregular galaxies, as well as interactions, e.g., NGC 5194 (M51A). We note that S⁴G does not include many ellipticals in its selection and that — as with all morphological selection — some objects are selected because of image artifacts. In the case of IRAC images, pulldown columns due to a bright nearby star seem to do so from time to time, even though most of these are masked in the pipeline products. A quick visual check of the selected objects reveals some are indeed selected for that reason.

Our sample of 2349 galaxies is the full, volume- and mass-limited, sample of S⁴G but the values in Table 3 show that not every criterion translates well to Spitzer IRAC morphologies for tidally disturbed galaxies defined for other wavelengths. Only the G_M and G-M₂₀ criteria select a similar fraction of galaxies to be interacting in the local Universe as previous studies (~ 5% Darg et al. 2010; Knapen & James 2009; Holwerda et al. 2011b, Laine et al. (*in preparation*)), using techniques such as visual inspection of the SDSS images and morphological selection of disturbed HI maps.

These two criteria (G_M and G-M₂₀) predominantly select later types as “unusual” so these selection criteria may not work as well for the early-type galaxies observed in the near-infrared that are interacting. Combined with the relative lack of early-types in the S⁴G sample, we note that these two morphological selections to estimate a merger rate for the later-types from S⁴G.

6.2. Arp Atlas

In our 2349 galaxies, there are 104 galaxies out of the 338 in the Arp catalog of peculiar galaxies (Arp 1966, 1995). Figure 13 shows the distributions of these 104 galaxies. The first thing to note is that hardly any are selected by the morphological criteria for disturbed systems, i.e., “peculiar” does not equate “disturbed” in the quantified morphology sense. This is to caution the use

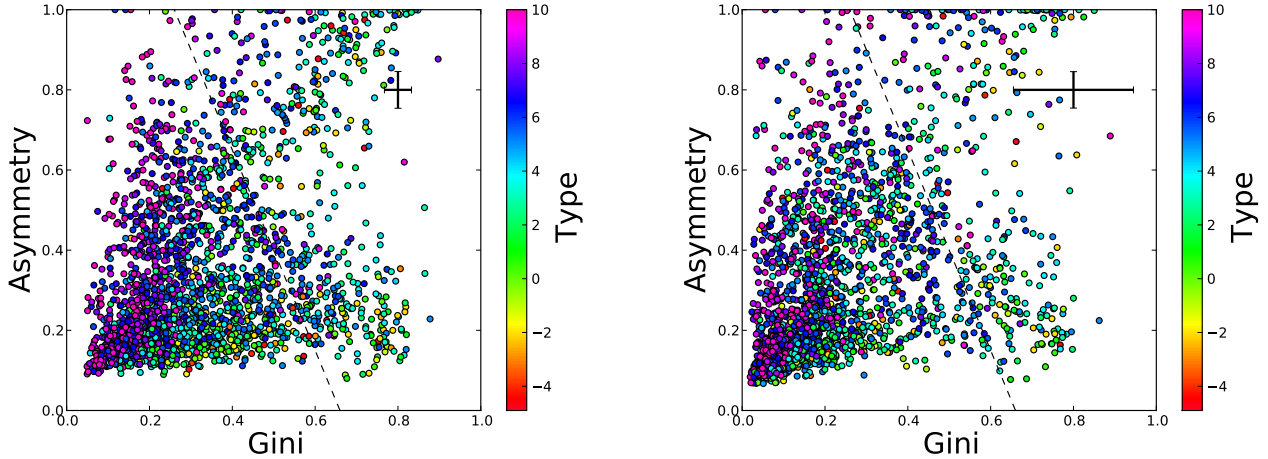


Figure 10. The relation between Gini and Asymmetry for 3.6 (left) and 4.5 μm (right) for S⁴G galaxies. The dashed line is the interaction criterion from Lotz et al. (2004) (equation 15). Galaxies to the right and above this line are candidate interactions.

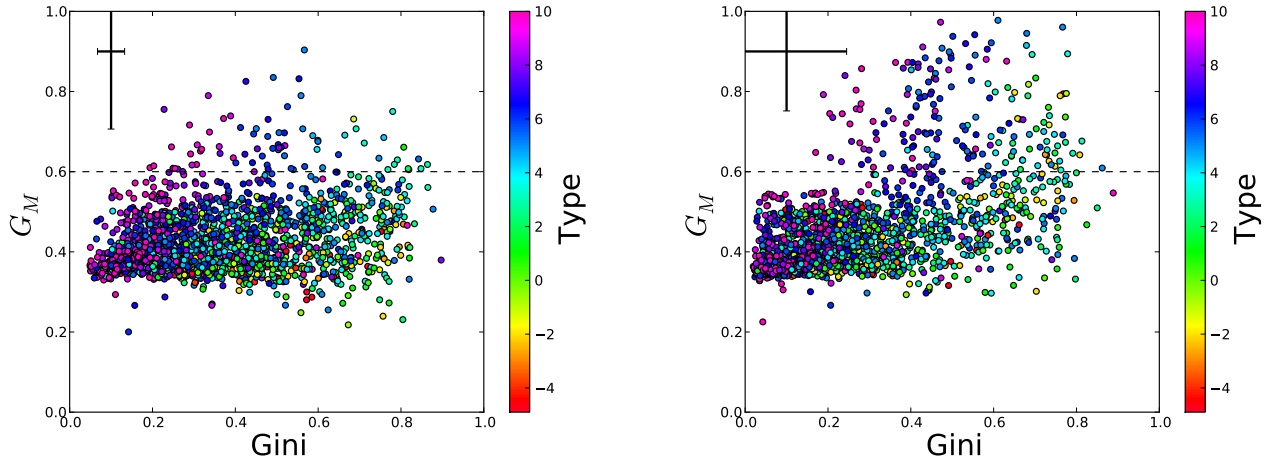


Figure 11. The relation between Gini and G_M for 3.6 (left) and 4.5 μm (right) for S⁴G galaxies. The horizontal dashed line is the interaction criterion for HI maps from Holwerda et al. (2011a) (equation 16). Galaxies above the line are candidate interactions.

of a selection of galaxies with outlying morphologies. Galaxies with a peculiar appearance in the visible light are not those identified in outlying morphological parameters in the near-infrared.

And the second thing to note is that while these morphological parameters may contain enough information to approximately morphologically classify and single out tidally disturbed systems, they do not contain enough power to single out galaxies with peculiar properties. That remains in the scope of visual classification (Laine et al. *in preparation*).

6.3. [3.6–4.5] Color

One option that may influence the difference in the Concentration- M_{20} relations between the 3.6 and 4.5 μm images is a contribution from the PAH feature at 3.1 μm to the 3.6 μm images or relatively brighter hot dust emission in the 4.5 μm channel. Figure 14 shows the residual from the C- M_{20} fit as a function of global [3.6–4.5] color from Munoz-Mateos et al. (*in preparation*).

The majority of S⁴G galaxies lie in a narrow range of color [3.6–4.5] = -0.7 to -0.3 with a mean color of -0.427. The most extreme colors paradoxically have the smallest residuals and the morphological outliers (residual >1.5) have typical colors. Table 2 also lists the correlation between the morphological parameters and the [3.6–4.5] color. The Spearman values are as close to unrelated as one can expect.

In our opinion, this points to a scenario where one or more bright HII regions or other features, likely at higher radii, displace the galaxy from the C- M_{20} morphological relation but not from the typical [3.6–4.5] color, i.e., there is not enough hot dust or PAH emission in the bright HII regions to change the galaxy-wide color but enough flux (at a greater distance to the center) to change the appearance.

7. LOPSIDEDNESS

Morphological lopsidedness is a distinct displacement of the disk with respect to its apparent center (photomet-

Table 4

The Spearman ranking of the relations between the Lopsidedness parameterizations from Zaritsky et al. (2013b) and the morphological parameters in 3.6 μm and 4.5 μm for the available subsample of 187 galaxies. The absolute z-values of significance for each of Spearman rankings are noted between parentheses.

Lopsidedness	C	A	S	M_{20}	G	G_M
3.6 μm						
$\langle A_1 \rangle_i$	-0.30 (3.86)	-0.03 (0.39)	0.12 (1.50)	0.35 (4.45)	-0.22 (2.81)	0.03 (0.34)
$\langle A_2 \rangle_i$	-0.31 (3.99)	-0.20 (2.48)	0.09 (1.15)	0.29 (3.61)	-0.27 (3.40)	-0.02 (0.31)
$\langle A_1 \rangle_o$	-0.21 (2.61)	-0.11 (1.37)	0.19 (2.35)	0.18 (2.30)	-0.19 (2.31)	0.03 (0.41)
$\langle A_2 \rangle_o$	-0.48 (6.38)	-0.16 (1.93)	0.16 (2.03)	0.39 (5.09)	-0.40 (5.17)	0.00 (0.05)
4.5 μm						
$\langle A_1 \rangle_i$	-0.22 (2.76)	-0.10 (1.26)	0.02 (0.22)	0.22 (2.72)	-0.18 (2.18)	-0.16 (1.96)
$\langle A_2 \rangle_i$	-0.24 (2.94)	-0.20 (2.47)	0.01 (0.18)	0.13 (1.58)	-0.17 (2.14)	-0.19 (2.39)
$\langle A_1 \rangle_o$	-0.12 (1.52)	-0.09 (1.16)	0.09 (1.16)	0.07 (0.86)	-0.10 (1.21)	-0.10 (1.26)
$\langle A_2 \rangle_o$	-0.38 (4.94)	-0.25 (3.19)	-0.05 (0.65)	0.32 (4.13)	-0.32 (4.04)	-0.18 (2.23)

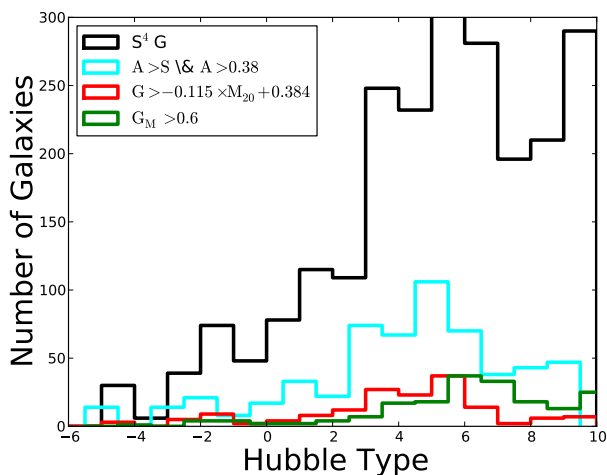


Figure 12. The histogram of Hubble types for the full S⁴G sample and those galaxies selected by the four criteria as disturbed. The Asymmetry-Smoothness criterion (equation 13) from Conselice (2003), the Gini- M_{20} criterion (equation 14) from Lotz et al. (2004) and the G_M (equation 16) and Concentration- M_{20} (equation 18) criteria from Holwerda et al. (2011a).

ric or kinematic). The effect was initially noticed in HI and then in stellar disks (see for a comprehensive review, Jog & Combes 2009). The first comprehensive study on stellar disks was by Rix & Zaritsky (1995) and a study on S⁴G was just completed (Zaritsky et al. 2013b). The motivation for this analysis is very similar to our own: the advent of large surveys, ample computing power, and the desire for more reproducible results in morphological studies.

Zaritsky et al. (2013b) perform an azimuthal Fourier decomposition of the luminosity in circular annuli at two radial intervals on the S⁴G data. Similar to Rix & Zaritsky (1995), they calculate the relative strength of the first and second Fourier component: $\langle A_1 \rangle$ is the average of A_1/A_0 and $\langle A_2 \rangle$ is the average of A_2/A_0 . A_m is the amplitude of the m mode ($m=0-4$) in the image. The $m=0$ mode corresponds to the central amplitude (concentration of flux in the center), the $m=1$ mode to a displacement of the flux in one direction with respect to the center, i.e., lopsidedness, and $m=2$ is a axisymmetric displacement of flux with respect to the center, e.g., a strong bar.

Zaritsky et al. (2013b) report these values calculated between 1.5 to 2.5 disk scale-lengths ($\langle A_1 \rangle_i$ & $\langle A_2 \rangle_i$), and 2.5 to 3.5 scale lengths ($\langle A_1 \rangle_o$ & $\langle A_2 \rangle_o$) in the S⁴G data. The deep S⁴G data allows the additional measurement at larger radii compared to the earlier studies. The $m = 1$ modes ($\langle A_1 \rangle_i$ and $\langle A_1 \rangle_o$) trace the lopsidedness of the disk.

There is only a weak link in HI between the C, A, S, Gini, M_{20} and G_M parameters and the presence of lopsidedness (Holwerda et al. 2011a). However, the new morphology catalog and the lopsidedness parameterization for an S⁴G subsample, allows us to compare the relation between the strength of lopsidedness and the morphology parameters. Figures 17, 21, 20, 23 show our catalog color coded with the $m=1$ and $m=2$ modes at both radii. They illustrate that the lopsidedness sample does not cover the full morphological parameter space, with only few points above the traditional interacting criteria, e.g., equation 15 or 16. Figures 18 and 19 show the direct relation between the $m=1$ and $m=2$ modes with the morphology parameters, for the inner and 22 and 24 for the outer ring respectively. Table 6.3 lists the Spearman ranking of all our parameters with the $m=1$ and $m=2$ modes at both radii for both wavelengths. Between lopsidedness ($m=2$) at either radii and most of our parameters, there is only a weak correlation or none at all. The strongest anti-correlation is between $\langle A_1 \rangle_i$ and Concentration and strongest correlation is between $\langle A_1 \rangle_i$ and M_{20} . The concentration and M_{20} parameters are equally strongly correlated to the $m=2$ mode. The lack of a strong relation between the morphology parameters and the Fourier components shows that Asymmetry and lopsidedness are not related phenomena, i.e., an asymmetric galaxy need not be lopsided and a lopsided one not strongly asymmetric.

8. CONCLUDING REMARKS

Based on 3.6 and 4.5 μm images of 2349 galaxies from the S⁴G survey, we can conclude that:

1. There is a close relation for normal galaxies between their concentration (C_{82}) and M_{20} (Figure 7), at 3.6 μm images.
2. To first order, a Hubble type can be found from M_{20} (or C_{82}): samples of early and late types could be identified using M_{20} alone (Figure 9) but sub-type classification is impossible.

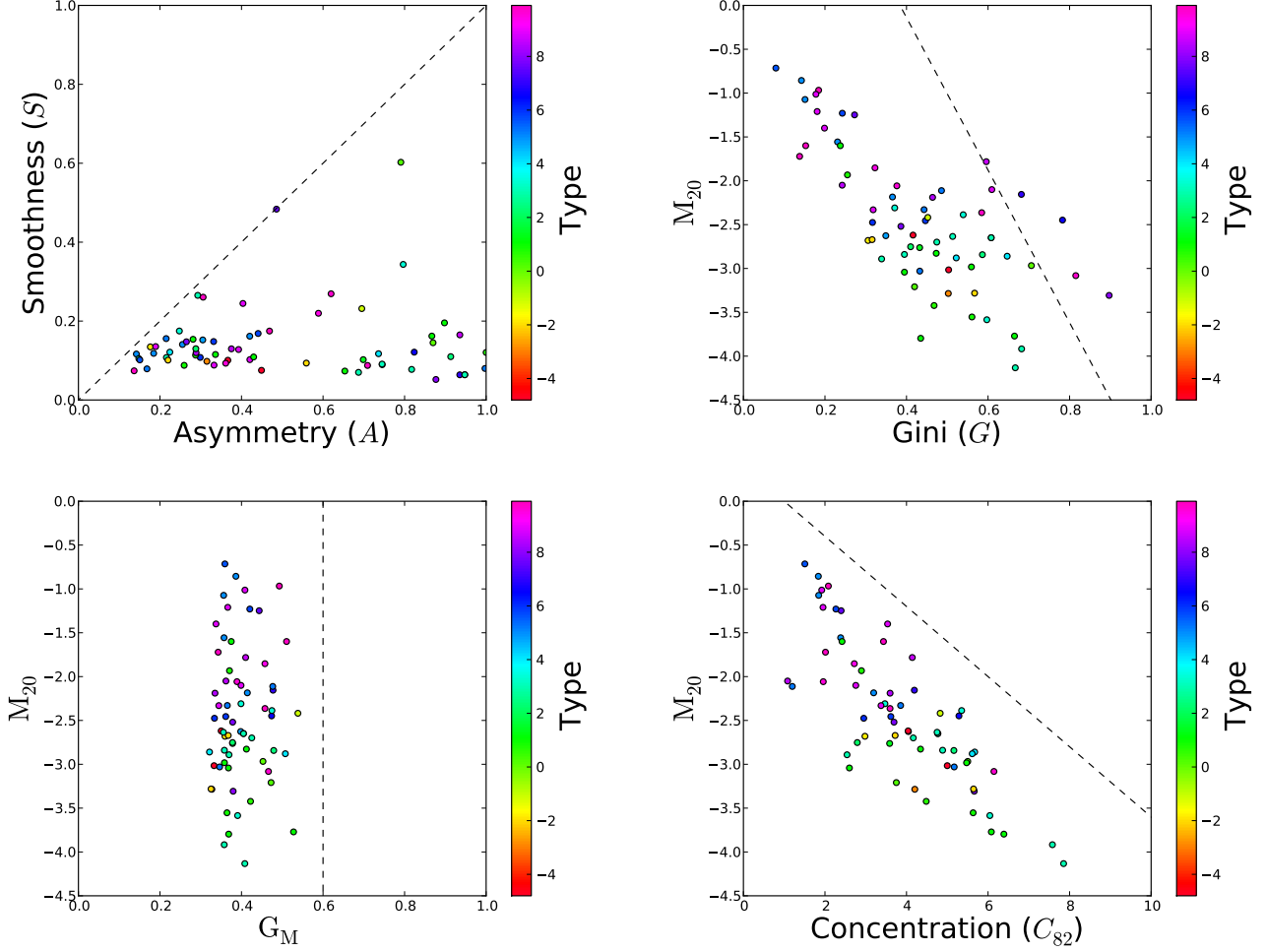


Figure 13. The distribution of morphological parameters in $3.6 \mu\text{m}$ of the 104 Arp galaxies in our sample. Dashed lines are the selection criteria (equation 13–14) for disturbed galaxies: the Asymmetry-Smoothness criterion from Conselice (2003) (equation 13), the Gini- M_{20} criterion from Lotz et al. (2004) (equation 14), the G_M and Concentration- M_{20} criteria from Holwerda et al. (2011a) (equations 16 and 18 respectively). Only the Gini- M_{20} criterion selects a sizable number of Arp atlas galaxies based on their S⁴G morphology.

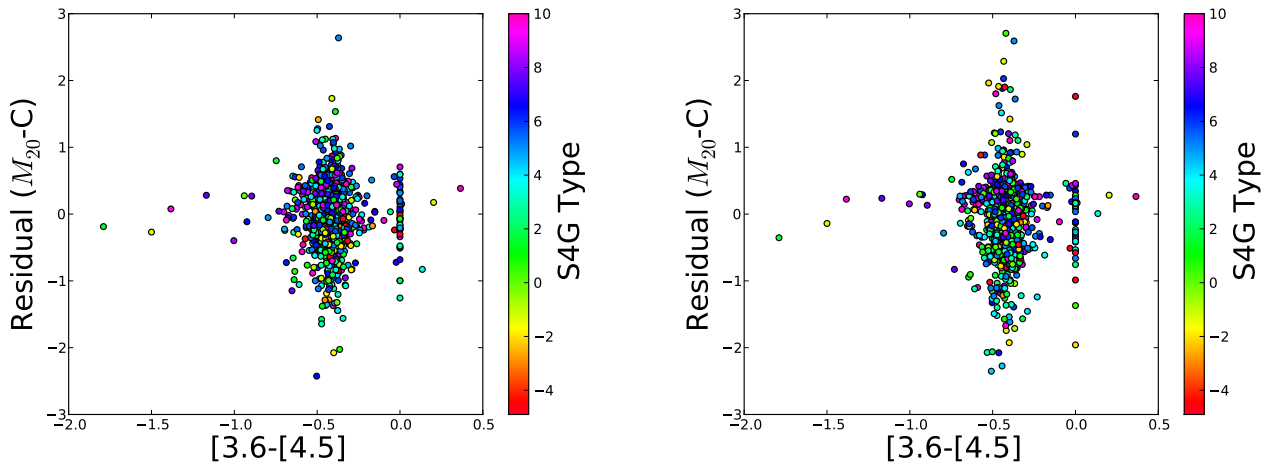


Figure 14. The residual after subtracting the Concentration- M_{20} relations in equations 9 at $3.6 \mu\text{m}$ 1 (left) and 10 for $4.5 \mu\text{m}$ (right panel) as a function of global galaxy color from Muñoz-Mateos et al. (*in preparation*). Points are color-coded by HyperLEDA type (Paturel et al. 2003). The color range for the S⁴G is galaxies is very narrow. Those with extreme colors have few outliers and those with great residuals, a typical color.

3. Four morphological criteria work to identify “disturbed” or unique systems (Table 3), but each selects a different subgroup of our sample. Only the G_M and $G-M_{20}$ criteria select close to the typical merger fraction of the local Universe. The $C-M_{20}$ criterion provides a lower limit for the interaction fraction.
4. General morphological type, i.e., early vs late, can be inferred from M_{20} parameter in $3.6 \mu\text{m}$ but not finer than that.
5. The lack of a relation between the Concentration– M_{20} residual and global galaxy color points to distinct substructures causing the residual, not global hot dust or PAH contributions.
6. There is only a weak link between Concentration and M_{20} and lopsidedness in a subsample (Table 6.3) and these parameters are not suited to detection of this phenomenon.

ACKNOWLEDGEMENTS

The authors thank the entire S⁴G team for their efforts in this project and the anonymous referee for his or her insightful comments for the improvement of the manuscript. The lead author thanks the European Space Agency for the support of the Research Fellowship program. This work was co-funded under the Marie Curie Actions of the European Commission (FP7-COFUND). We acknowledge financial support to the DAGAL network from the People Programme (Marie Curie Actions) of the European Union’s Seventh Framework Programme FP7/2007-2013/ under REA grant agreement number PITN-GA-2011-289313. E.A. and A.B. acknowledge the CNES (Centre National d’Etudes Spatiales - France) for financial support. They also acknowledge the support from the FP7 Marie Curie Actions of the European Commission, via the Initial Training Network DAGAL under REA grant agreement n 289313. This work is based on observations made with the *Spitzer Space Telescope*, which is operated by the Jet Propulsion Laboratory, California Institute of Technology under a contract with NASA. This research has made use of the NASA/IPAC Extragalactic Database (NED) which is operated by the Jet Propulsion Laboratory, California Institute of Technology, under contract with the National Aeronautics and Space Administration. This research has made use of NASA’s Astrophysics Data System. We acknowledge the usage of the HyperLEDA database (<http://leda.univ-lyon1.fr> Paturel et al. 2003).

REFERENCES

- Abraham, R. G., & Merrifield, M. R. 2000, *AJ*, 120, 2835
 Abraham, R. G. et al. 2003, *ApJ*, 588, 218
 Arp, H. 1966, *ApJS*, 14, 1
 Arp, H. C. 1995, *VizieR Online Data Catalog*, 7074, 0
 Bakes, E. L. O. et al. 2001, *ApJ*, 560, 261
 Ball, N. M. et al. 2004, *MNRAS*, 348, 1038
 Bendo, G. J. et al. 2007, *MNRAS*, 380, 1313
 Bershad, M. A. et al. 2000, *AJ*, 119, 2645
 Bertin, E., & Arnouts, S. 1996, *A&AS*, 117, 393, provided by the NASA Astrophysics Data System
 Bundy, K. et al. 2005, *ApJ*, 625, 621
 Buta, R. J. et al. 2010, *ApJS*, 190, 147
 Cassata, P. et al. 2005, *MNRAS*, 357, 903
 Comerón, S. et al. 2011a, *ApJ*, 741, 28
 —. 2011b, *ApJ*, 738, L17
 —. 2012, *ApJ*, 759, 98
 —. 2011c, *ApJ*, 729, 18
 Conselice, C. J. 2003, *ApJS*, 147, 1
 Conselice, C. J. et al. 2003, *AJ*, 126, 1183
 —. 2000, *ApJ*, 529, 886
 —. 2005, *ApJ*, 620, 564
 —. 2008, *MNRAS*, 383, 1366
 —. 2009, *MNRAS*, 361
 Darg, D. W. et al. 2010, *MNRAS*, 401, 1043
 de Blok, W. J. G. et al. 2008, *AJ*, 136, 2648
 de Vaucouleurs, G. et al. 1991, *Third Reference Catalogue of Bright Galaxies (Volume 1-3, XII, 2069 pp. 7* figs., Springer-Verlag Berlin Heidelberg New York)
 Domingue, D. L. et al. 2000, *ApJ*, 545, 171
 Elmegreen, D. M. et al. 2011, *ApJ*, 737, 32
 Erroz-Ferrer, S. et al. 2012, *MNRAS*, 427, 2938
 Eskew, M. et al. 2012, *AJ*, 143, 139
 Fazio, G. G. et al. 2004, *ApJS*, 154, 10
 Flagey, N. et al. 2006, in *Astronomical Society of the Pacific Conference Series, Vol. 357, Astronomical Society of the Pacific Conference Series*, ed. L. Armus & W. T. Reach, 85
 Fortson, L. et al. 2012, *Galaxy Zoo: Morphological Classification and Citizen Science*, ed. M. J. Way, J. D. Scargle, K. M. Ali, & A. N. Srivastava, 213–236
 Frei, Z. et al. 1996, *AJ*, 111, 174
 Holwerda, B. W. 2005, *astro-ph/0512139*
 Holwerda, B. W. et al. 2013, *MNRAS*, 433, 47
 —. 2007a, *AJ*, 134, 2226
 Holwerda, B. W., & Keel, W. C. 2013, *ArXiv e-prints*
 Holwerda, B. W. et al. 2007b, *AJ*, 134, 2385
 —. 2009, *AJ*, 137, 3000
 —. 2007c, *AJ*, 134, 1655
 —. 2011a, *MNRAS*, 416, 2426
 —. 2011b, *MNRAS*, 416, 2437
 —. 2011c, *MNRAS*, 416, 2401
 —. 2011d, *MNRAS*, 416, 2415
 —. 2011e, *MNRAS*, 416, 2447
 —. 2012, *MNRAS*, 427, 3159
 Hoyle, B. et al. 2011, *MNRAS*, 415, 3627
 Huertas-Company, M. et al. 2009, *A&A*, 497, 743
 Jog, C. J., & Combes, F. 2009, *Phys. Rep.*, 471, 75
 Jooe, S. et al. 2009, *ApJ*, 697, 1971
 Keel, W. C. et al. 2013, *PASP*, 125, 2
 Keel, W. C., & White, III, R. E. 2001a, *AJ*, 121, 1442
 —. 2001b, *AJ*, 122, 1369
 Kennicutt, R. C. et al. 2003, *PASP*, 115, 928
 Kent, S. M. 1985, *ApJS*, 59, 115
 Kim, T. et al. 2012, *ApJ*, 753, 43
 Knapen, J. H., & James, P. A. 2009, *ApJ*, 698, 1437
 Kormendy, J., & Bender, R. 2012, *ApJS*, 198, 2
 Lahav, O. et al. 1996, *MNRAS*, 283, 207
 Lintott, C. J. et al. 2008, *MNRAS*, 389, 1179
 Lisker, T. 2008, *ApJS*, 179, 319
 López-Sanjuan, C. et al. 2009a, *ApJ*, 694, 643
 —. 2009b, *A&A*, 501, 505
 Lotz, J. M. et al. 2008, *ApJ*, 672, 177
 —. 2004, *AJ*, 128, 163
 Lu, N. et al. 2003, *ApJ*, 588, 199
 Malin, D. F. 1978, *Nature*, 276, 591
 Masters, K. L. et al. 2010, *MNRAS*, 404, 792
 —. 2012, *MNRAS*, 424, 2180
 —. 2011, *MNRAS*, 411, 2026
 Meidt, S. E. et al. 2012a, *ApJ*, 744, 17
 —. 2012b, *ApJ*, 748, L30
 Mentuch, E. et al. 2009, *ApJ*, 706, 1020
 —. 2010, *ApJ*, 725, 1971
 Molinari, E., & Smareglia, R. 1998, *A&A*, 330, 447
 Muñoz-Mateos, J. C. et al. 2009, *ApJ*, 703, 1569
 Pahre, M. A. et al. 2004a, *ApJS*, 154, 235
 —. 2004b, *ApJS*, 154, 229
 Paturel, G. et al. 2003, *A&A*, 412, 45
 Ravindranath, S. et al. 2006, *ApJ*, 652, 963
 Rix, H.-W., & Zaritsky, D. 1995, *ApJ*, 447, 82
 Sandage, A. 2005, *ARA&A*, 43, 581

- Scarlata, C. et al. 2007, *ApJS*, 172, 406
Schade, D. et al. 1995, *ApJ*, 451, L1
Sérsic, J. L. 1968, *Atlas de galaxias australes*, ed. Sérsic, J. L.
Sheth, K. et al. 2010, *PASP*, 122, 1397
Skibba, R. A. et al. 2009, *MNRAS*, 399, 966
—. 2012, *MNRAS*, 423, 1485
—. 2011, *ArXiv e-prints*
Taylor-Mager, V. A. et al. 2007, *ApJ*, 659, 162
Thilker, D. A. et al. 2007, *ApJS*, 173, 538
Trujillo, I. et al. 2007, *MNRAS*, 382, 109
Werner, M. W. et al. 2004, *ApJS*, 154, 1
White, R. E., & Keel, W. C. 1992, *Nature*, 359, 129
White, III, R. E. et al. 2000, *ApJ*, 542, 761
Yan, H. et al. 2005, *ApJ*, 634, 109
Zaritsky, D. et al. 2013a, *ArXiv e-prints*
—. 2013b, *ApJ*, 772, 135
Zibetti, S., & Groves, B. 2011, *MNRAS*, 417, 812

TABLES OF MORPHOLOGICAL PARAMETERS

Table 5The morphological parameters at 3.6 μm for the 2349 S^4G galaxies. Full table is available in the *electronic edition*.

Name	Gini	M_{20}	C82	A	S	E	G_M
ESO011-005	0.306 \pm 0.009	-2.359 \pm 0.082	2.190 \pm 0.108	1.206 \pm 0.042	0.741 \pm 0.017	0.068 \pm 0.010	0.432 \pm 0.004
ESO012-010	0.372 \pm 0.016	-1.959 \pm 0.091	2.879 \pm 0.177	0.710 \pm 0.136	0.332 \pm 0.035	0.421 \pm 0.014	0.438 \pm 0.014
ESO012-014	0.208 \pm 0.009	-0.906 \pm 0.054	1.451 \pm 0.082	1.347 \pm 0.035	0.850 \pm 0.033	0.041 \pm 0.026	0.532 \pm 0.005
ESO013-016	0.476 \pm 0.005	-1.993 \pm 0.105	3.734 \pm 0.177	0.898 \pm 0.095	0.477 \pm 0.035	0.070 \pm 0.028	0.530 \pm 0.005
ESO015-001	0.316 \pm 0.006	-2.281 \pm 0.145	1.025 \pm 0.223	1.111 \pm 0.152	0.713 \pm 0.046	0.084 \pm 0.024	0.515 \pm 0.004
ESO026-001	0.447 \pm 0.007	-2.108 \pm 0.140	3.096 \pm 0.145	1.035 \pm 0.067	0.456 \pm 0.025	0.042 \pm 0.017	0.436 \pm 0.007
ESO027-001	0.637 \pm 0.006	-2.550 \pm 0.103	4.374 \pm 0.289	1.783 \pm 0.044	0.252 \pm 0.045	0.250 \pm 0.026	0.490 \pm 0.006
ESO027-008	0.631 \pm 0.006	-2.671 \pm 0.080	3.768 \pm 0.331	1.859 \pm 0.011	0.296 \pm 0.039	0.323 \pm 0.018	0.507 \pm 0.005
ESO048-017	0.263 \pm 0.008	-1.741 \pm 0.096	1.914 \pm 0.122	1.235 \pm 0.028	0.756 \pm 0.024	0.037 \pm 0.014	0.468 \pm 0.003
ESO054-021	0.440 \pm 0.010	-2.018 \pm 0.083	3.614 \pm 0.125	0.840 \pm 0.070	0.330 \pm 0.038	0.238 \pm 0.026	0.491 \pm 0.009
ESO079-003	0.848 \pm 0.004	-1.866 \pm 0.313	4.457 \pm 0.449	1.998 \pm 0.001	0.138 \pm 0.035	0.128 \pm 0.075	0.608 \pm 0.003
ESO079-005	0.504 \pm 0.008	-1.702 \pm 0.166	1.564 \pm 0.364	0.881 \pm 0.178	0.368 \pm 0.069	0.186 \pm 0.036	0.667 \pm 0.005
ESO079-007	0.419 \pm 0.006	-2.501 \pm 0.097	3.327 \pm 0.190	0.926 \pm 0.150	0.543 \pm 0.038	0.066 \pm 0.019	0.479 \pm 0.003
ESO085-014	0.446 \pm 0.005	-1.334 \pm 0.093	1.107 \pm 0.129	1.869 \pm 0.017	0.538 \pm 0.037	0.277 \pm 0.021	0.600 \pm 0.003
ESO085-030	0.734 \pm 0.008	-2.731 \pm 0.291	6.022 \pm 0.360	0.380 \pm 0.515	0.181 \pm 0.058	0.120 \pm 0.036	0.570 \pm 0.006
ESO085-047	0.199 \pm 0.005	-1.124 \pm 0.028	1.804 \pm 0.037	0.794 \pm 0.030	0.404 \pm 0.008	0.021 \pm 0.005	0.394 \pm 0.003
ESO107-016	0.183 \pm 0.006	-0.693 \pm 0.008	1.587 \pm 0.011	0.588 \pm 0.026	0.267 \pm 0.005	0.013 \pm 0.012	0.401 \pm 0.007
ESO114-007	0.361 \pm 0.009	-1.994 \pm 0.289	3.453 \pm 0.360	1.221 \pm 0.167	0.626 \pm 0.063	0.087 \pm 0.038	0.663 \pm 0.005
ESO115-021	0.303 \pm 0.003	-1.673 \pm 0.053	3.163 \pm 0.090	1.955 \pm 0.008	0.649 \pm 0.021	0.528 \pm 0.009	0.575 \pm 0.002
ESO116-012	0.408 \pm 0.006	-1.985 \pm 0.078	0.410 \pm 0.063	1.235 \pm 0.018	0.252 \pm 0.009	0.568 \pm 0.007	0.476 \pm 0.004
ESO119-016	0.228 \pm 0.005	-1.356 \pm 0.037	1.717 \pm 0.052	1.258 \pm 0.032	0.683 \pm 0.015	0.025 \pm 0.010	0.461 \pm 0.003
ESO120-012	0.252 \pm 0.005	-1.144 \pm 0.048	1.906 \pm 0.072	0.816 \pm 0.038	0.414 \pm 0.010	0.029 \pm 0.009	0.421 \pm 0.006
ESO120-021	0.186 \pm 0.006	-1.099 \pm 0.030	1.851 \pm 0.036	0.840 \pm 0.041	0.432 \pm 0.011	0.025 \pm 0.008	0.401 \pm 0.005
ESO145-025	0.195 \pm 0.004	-0.874 \pm 0.013	1.674 \pm 0.034	0.900 \pm 0.013	0.427 \pm 0.007	0.035 \pm 0.008	0.412 \pm 0.003
ESO146-014	0.172 \pm 0.008	-0.796 \pm 0.009	1.713 \pm 0.028	1.195 \pm 0.021	0.388 \pm 0.010	0.304 \pm 0.006	0.490 \pm 0.005
ESO149-001	0.349 \pm 0.004	-1.851 \pm 0.094	2.955 \pm 0.114	1.314 \pm 0.025	0.703 \pm 0.022	0.540 \pm 0.013	0.505 \pm 0.002
ESO149-003	0.338 \pm 0.014	-1.618 \pm 0.212	1.325 \pm 0.251	0.885 \pm 0.300	0.264 \pm 0.061	0.222 \pm 0.124	0.699 \pm 0.018
ESO150-005	0.240 \pm 0.005	-0.765 \pm 0.071	2.038 \pm 0.118	1.629 \pm 0.032	0.791 \pm 0.027	0.059 \pm 0.018	0.598 \pm 0.002
ESO154-023	0.303 \pm 0.004	-1.472 \pm 0.084	1.497 \pm 0.074	1.931 \pm 0.003	0.649 \pm 0.034	0.294 \pm 0.014	0.543 \pm 0.002
ESO157-049	0.758 \pm 0.007	-2.451 \pm 0.145	4.224 \pm 0.577	0.873 \pm 0.291	0.183 \pm 0.054	0.550 \pm 0.036	0.525 \pm 0.006
ESO159-025	0.160 \pm 0.004	-1.003 \pm 0.022	1.350 \pm 0.029	0.587 \pm 0.034	0.172 \pm 0.003	0.051 \pm 0.006	0.370 \pm 0.004
ESO187-035	0.167 \pm 0.002	-0.765 \pm 0.009	1.595 \pm 0.016	0.510 \pm 0.039	0.231 \pm 0.003	0.013 \pm 0.003	0.399 \pm 0.002
ESO187-051	0.166 \pm 0.002	-0.916 \pm 0.011	1.660 \pm 0.016	0.463 \pm 0.024	0.198 \pm 0.001	0.034 \pm 0.002	0.376 \pm 0.001
ESO202-035	0.730 \pm 0.005	-2.036 \pm 0.183	4.413 \pm 0.417	1.392 \pm 0.073	0.261 \pm 0.054	0.275 \pm 0.041	0.529 \pm 0.004
ESO202-041	0.242 \pm 0.007	-2.099 \pm 0.211	1.598 \pm 0.128	1.423 \pm 0.091	0.906 \pm 0.060	0.018 \pm 0.029	0.561 \pm 0.004
ESO234-043	0.209 \pm 0.004	-1.079 \pm 0.018	1.463 \pm 0.028	0.632 \pm 0.057	0.255 \pm 0.005	0.031 \pm 0.004	0.387 \pm 0.003
ESO234-049	0.289 \pm 0.013	-1.927 \pm 0.050	2.681 \pm 0.077	0.565 \pm 0.058	0.169 \pm 0.013	0.014 \pm 0.013	0.371 \pm 0.009
ESO236-039	0.194 \pm 0.006	-0.963 \pm 0.018	1.884 \pm 0.035	0.593 \pm 0.053	0.299 \pm 0.005	0.032 \pm 0.003	0.393 \pm 0.003
ESO237-049	0.223 \pm 0.005	-0.690 \pm 0.015	2.037 \pm 0.034	0.795 \pm 0.040	0.390 \pm 0.006	0.282 \pm 0.003	0.500 \pm 0.004
...

APPENDIX

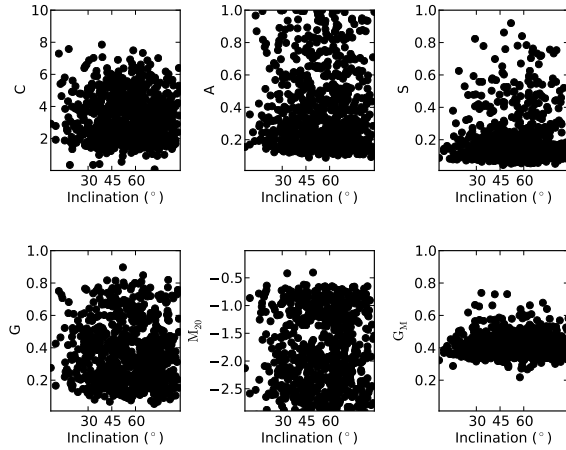


Figure 15. The six morphology parameters as a function of inclination. None of the morphological parameters relate closely to the inclination, not even Concentration.

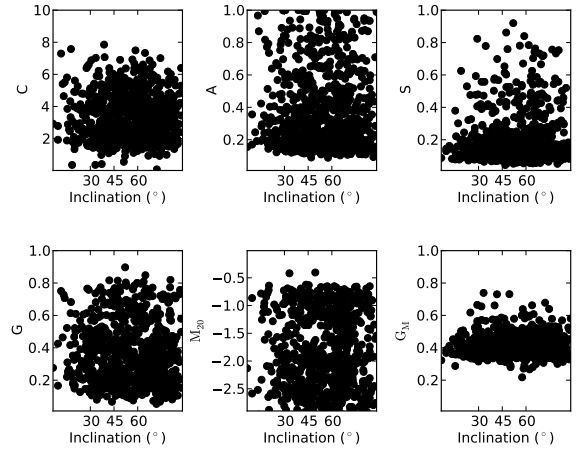


Figure 16. The six morphology parameters as a function of distance. None of the morphological parameters relate closely to the distance, not even Smoothness.

Table 3

The Spearman ranking of the relation between inclination or distance and the morphological parameters in either $3.6 \mu\text{m}$ or $4.5 \mu\text{m}$ images for our full sample. The absolute z-values of significance for each of Spearman rankings are noted between parentheses.

Type	C	A	S	M_{20}	G	G_M
3.6 μm						
Inclination ($^\circ$)	-0.07 (1.84)	-0.01 (0.29)	0.02 (0.44)	0.04 (1.12)	-0.07 (1.86)	-0.02 (0.58)
Distance (Mpc.)	-0.01 (0.40)	-0.02 (0.63)	-0.01 (0.46)	-0.01 (0.28)	-0.01 (0.40)	0.00 (0.04)
4.5 μm						
Inclination ($^\circ$)	-0.06 (1.52)	-0.03 (0.78)	0.02 (0.54)	0.03 (0.92)	-0.05 (1.31)	-0.00 (0.13)
Distance (Mpc.)	-0.01 (0.49)	-0.02 (0.52)	-0.04 (1.31)	0.02 (0.54)	-0.03 (1.07)	-0.03 (0.88)

Two possible systematics are explored here in this section: any relation between inclination and the morphological parameters and the effect of smoothing due to distance on the morphological parameters. Figure 15 show the lack of a relation between the inclination and any of the morphological parameters. One could expect a relation between disk inclination and concentration due to line-of-sight integration. However, no such relation in S^4G exists.

Similarly, one can expect a relation between Smoothness and distance. Galaxies further away appear smoother, which is the reasoning behind the surface brightness fluctuation distance measurement method. However, there is no such relation between the distances of the S^4G galaxies and their smoothness evident in Figure 16.

The Spearman rankings of the relations between inclination or distance and the S^4G morphology parameters bear out the lack of a relation (Table 3), albeit at low z-value confidences.

LOPSIDEDNESS

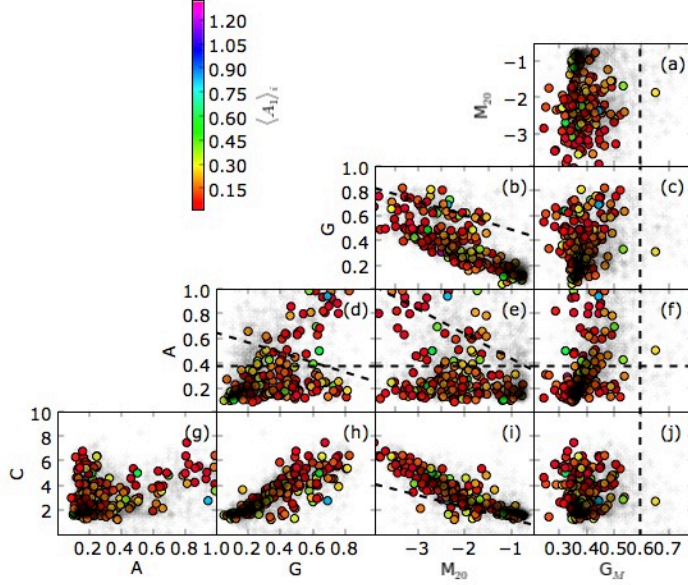


Figure 17. The distribution of the 3.6 μm morphological parameters color-coded with the $\langle A_1 \rangle_i$ parameter from Zaritsky et al. (2013b)) where available. The full S⁴G morphological sample is marked with gray crosses for reference. Dashed lines are the merger/interaction criteria: Sub-panels (a), (c), (f), and (j), the G_M criterion (equation 16) Sub-panel (b), the $G-M_{20}$ criterion from Lotz et al. (2004) (equation 14, sub-panel (d)), the $G-A$ criterion from Lotz et al. (2004) (equation 15), and sub-panels (d),(e) and (f), the horizontal line is the $A > 0.38$ criterion from Conselice (2003) (equation 13).

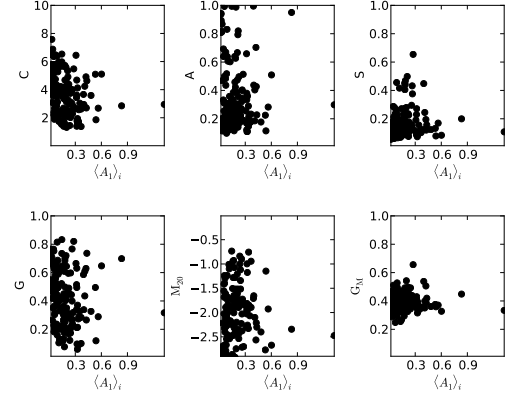


Figure 18. The direct relation between the *inner* (computed between 1.5 and 2.5 scale-lengths) $m=1$ mode from Zaritsky et al. (2013b)) and the six morphology parameters.

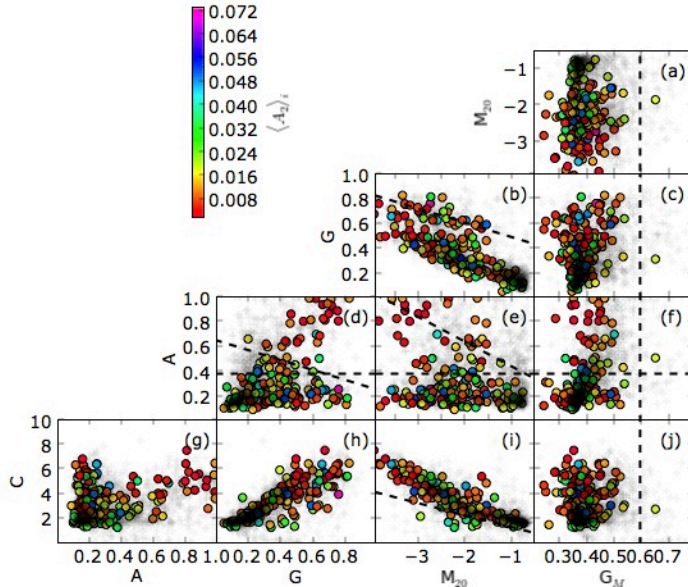


Figure 19. The direct relation between the *inner* (computed between 1.5 and 2.5 scale-lengths) $m=2$ mode from Zaritsky et al. (2013b)) and the six morphology parameters.

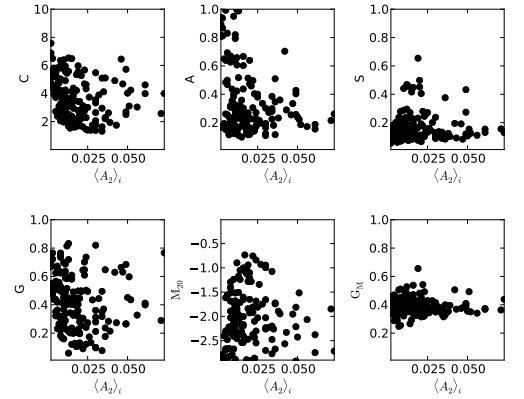


Figure 20. The distribution of the 3.6 μm morphological parameters color-coded with the $\langle A_2 \rangle_i$ parameter from Zaritsky et al. (2013b)) where available. The full S⁴G morphological sample is marked with gray crosses for reference. Dashed lines as in Figure 17.

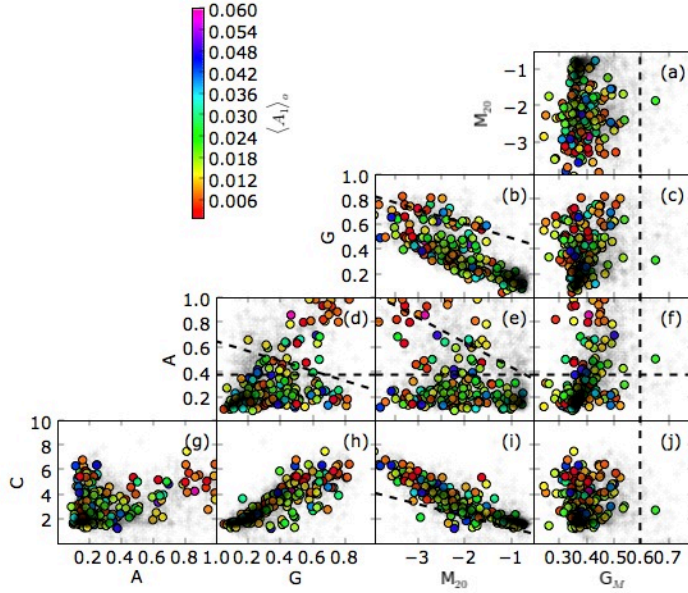


Figure 21. The distribution of the $3.6 \mu\text{m}$ morphological parameters color-coded with the $\langle A_1 \rangle_o$ parameter from Zaritsky et al. (2013b)) where available. The full S⁴G morphological sample is marked with gray crosses for reference. Dashed lines as in Figure 17.

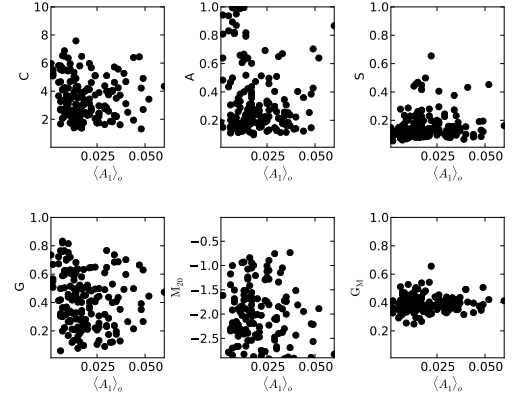


Figure 22. The direct relation between the *outer* (computed between 2.5 and 3.5 scale-lengths) $m=1$ mode from Zaritsky et al. (2013b)) and the six morphology parameters.

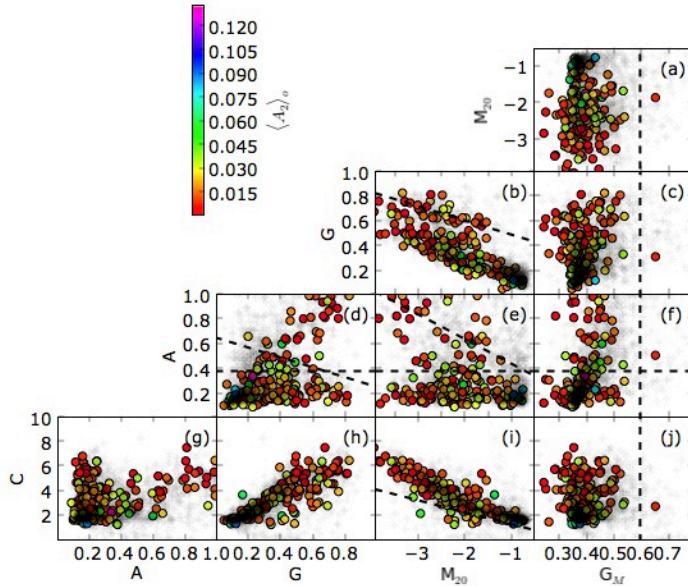


Figure 23. The distribution of the $3.6 \mu\text{m}$ morphological parameters color-coded with the $\langle A_2 \rangle_o$ parameter from Zaritsky et al. (2013b)) where available. The full S⁴G morphological sample is marked with gray crosses for reference. Dashed lines as in Figure 17.

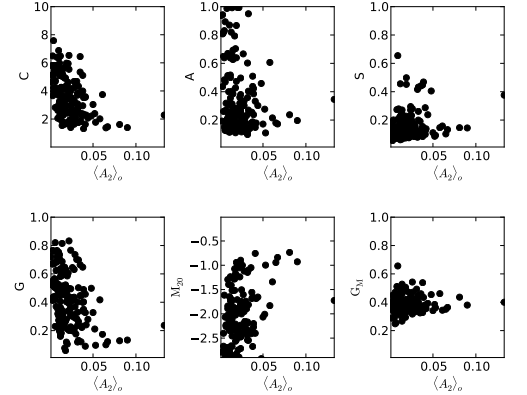


Figure 24. The direct relation between the *outer* (computed between 2.5 and 3.5 scale-lengths) $m=2$ mode from Zaritsky et al. (2013b)) and the six morphology parameters.